The Plant Cell, Vol. 26: 2689–2707, June 2014, www.plantcell.org

Rewiring Host Lipid Metabolism by Large Viruses Determines the Fate of *Emiliania huxleyi*, a Bloom-Forming Alga in the Ocean[C][W][OPEN]

Shilo Rosenwasser,[a,1] Michaela A. Mausz,[b,c,1] Daniella Schatz,[a] Uri Sheyn,[a] Sergey Malitsky,[a] Asaph Aharoni,[a] Eyal Weinstock,[a] Oren Tzfadia,[a] Shifra Ben-Dor,[d] Ester Feldmesser,[e] Georg Pohnert,[b] and Assaf Vardi[a,2]

[a] Department of Plant Sciences, Weizmann Institute of Science, Rehovot 7610001, Israel
[b] Institute of Inorganic and Analytical Chemistry/Bioorganic Analytics, Friedrich Schiller University Jena, 07743 Jena, Germany
[c] Leibniz Institute for Natural Product Research and Infection Biology, Hans Knöll Institute, 07745 Jena, Germany
[d] Bioinformatics and Biological Computing Unit, Weizmann Institute of Science, Rehovot 7610001, Israel
[e] The Nancy and Stephen Grand Israel National Center for Personalized Medicine, Weizmann Institute of Science, Rehovot 7610001, Israel

Marine viruses are major ecological and evolutionary drivers of microbial food webs regulating the fate of carbon in the ocean. We combined transcriptomic and metabolomic analyses to explore the cellular pathways mediating the interaction between the bloom-forming coccolithophore *Emiliania huxleyi* and its specific coccolithoviruses (*E. huxleyi* virus [EhV]). We show that EhV induces profound transcriptome remodeling targeted toward fatty acid synthesis to support viral assembly. A metabolic shift toward production of viral-derived sphingolipids was detected during infection and coincided with downregulation of host de novo sphingolipid genes and induction of the viral-encoded homologous pathway. The depletion of host-specific sterols during lytic infection and their detection in purified virions revealed their novel role in viral life cycle. We identify an essential function of the mevalonate-isoprenoid branch of sterol biosynthesis during infection and propose its downregulation as an antiviral mechanism. We demonstrate how viral replication depends on the hijacking of host lipid metabolism during the chemical "arms race" in the ocean.

INTRODUCTION

Phytoplankton are the foundation of the marine food web and are responsible for 50% of global photosynthesis (Field et al., 1998). The cosmopolitan coccolithophore *Emiliania huxleyi* (Prymnesiophyceae, Haptophyta) is a unicellular eukaryotic alga, responsible for the largest oceanic algal blooms, covering thousands of square kilometers (Holligan et al., 1993). Its intricate calcite exoskeleton accounts for approximately one-third of the total marine $CaCO_3$ production (Iglesias-Rodriguez et al., 2008). *E. huxleyi* is also a key producer of DMS, a bioactive gas with a significant climate-regulating role by enhancing cloud formation (Simó, 2001). Therefore, biotic interactions that regulate the fate of these blooms play a profound role in determining carbon flow in the ocean. Lytic viruses that infect algae were estimated to turn over more than a quarter of the total photosynthetically fixed carbon, thereby fueling microbial food webs, short-circuiting carbon transfer to higher trophic levels, and promoting export to the deep sea (Fuhrman, 1999; Suttle, 2007). Annual *E. huxleyi* spring blooms are frequently terminated by infection of a specific large double-stranded DNA (dsDNA) virus (*E. huxleyi* virus [EhV]) (Bratbak et al., 1993; Wilson et al., 2002). EhV belongs to the *Coccolithovirus*es (Schroeder et al., 2002), which is a group within the monophyletic *Phycodnaviridae*, a family of nucleocytoplasmic large DNA viruses (Van Etten et al., 2002). Members of the *Phycodnaviridae* can infect a wide range of algal species using diverse replication strategies. Most of these isolated viruses were shown to have a lytic replication cycle within their highly specific algal host. Nevertheless, a different lifestyle occurs in the brown macroalga *Ectocarpus siliculousus* virus (EsV-1) that only infects host gametophytes and integrates their genomic material into the host genome (Müller et al., 1998). A variety of EhV strains was isolated from different geographic regions, and variations in the host range were displayed by the different virus strains (Allen et al., 2007). However, the molecular mechanisms that underlie the variations in the host range displayed by a specific virus are unknown.

As a major evolutionary driver, marine viruses enhance the diversity of microbial life, affect species composition, and are responsible for widespread lateral gene transfer with their hosts. Recent reports highlighted a novel genomic inventory found in marine viruses that can encode auxiliary metabolic genes previously thought to be restricted to their host genomes. Thus, these genes can expand viral metabolic capabilities and energy transfer between host cells and their environment (Hurwitz et al.,

[1] These authors contributed equally to this work.
[2] Address correspondence to assaf.vardi@weizmann.ac.il.
The author responsible for distribution of materials integral to the findings presented in this article in accordance with the policy described in the Instructions for Authors (www.plantcell.org) is: Assaf Vardi (assaf.vardi@weizmann.ac.il).
[C] Some figures in this article are displayed in color online but in black and white in the print edition.
[W] Online version contains Web-only data.
[OPEN] Articles can be viewed online without a subscription.
www.plantcell.org/cgi/doi/10.1105/tpc.114.125641

2013; Enav et al., 2014). Genome analysis of EhV revealed a cluster of putative sphingolipid biosynthetic genes (Wilson et al., 2005), a pathway never before described in a viral genome. Glycosphingolipids, a subgroup of sphingolipids, are common constituents of membrane lipids and lipid rafts in eukaryotes. EhV is enveloped by lipid membranes (Mackinder et al., 2009), which are composed mainly of viral glycosphingolipids (vGSLs) (Fulton et al., 2014). These bioactive lipids can induce host programmed cell death (PCD) in lytic infected cells (Vardi et al., 2009, 2012). Indeed, during lytic infection, EhV can trigger hallmarks of PCD, including the production of reactive oxygen species (Evans et al., 2006; Vardi et al., 2012), induction of caspase activity, metacaspase expression, and compromised membrane integrity (Bidle et al., 2007; Vardi et al., 2012).

Viruses infecting higher plants are typically small RNA viruses that encode only a few genes; therefore, their life cycle is tightly integrated with and dependent on the cellular processes of their host plants (Roossinck, 1997). In contrast, large DNA viruses, which infect eukaryotic algae, are large dsDNA viruses with genomes ranging from 160 to 560 kb with up to 600 protein-encoding genes. Thus, these viruses require substantial amounts of building blocks, such as fatty acids, amino acids, and nucleotides, to facilitate replication and assembly. Nevertheless, a fundamental understanding of how giant viruses with high burst sizes like EhV rewire host metabolism to support their unique life cycle is lacking.

The advent of transcriptomic and metabolomic methods enables the exploration of complex metabolic and biosynthetic pathways that are central to host–pathogen interactions (Schauer and Fernie, 2006; Westermann et al., 2012; Zhao et al., 2013). In this article, we establish an attractive model system, using *E. huxleyi* as an ecologically important host and its lytic and nonlytic viruses. We provide a comprehensive view of the cellular processes central to host–virus interactions by detecting alterations in gene expression patterns and metabolic profiles during infection. Our data demonstrate how rapid remodeling in host primary metabolism redirects essential substrates to viral-derived sphingolipid biosynthesis as well as the central role of sterol metabolism in viral assembly and host defense.

RESULTS

Infection Dynamics of *E. huxleyi* and Its Specific Viruses

We exposed *E. huxleyi* (strain CCMP2090) to its lytic (EhV201) and nonlytic (EhV163) viruses and followed its dynamics over the time course of infection (see Supplemental Figure 1 for experimental setup). Cultures infected with EhV201 showed growth arrest and subsequently lysed, while cultures infected with EhV163 grew exponentially with cell abundances comparable to the control (Figures 1A and 1B). Induction of cell death was observed only during lytic infection with EhV201 (Figure 1C). Transmission electron microscopy (TEM) revealed degradation of the nucleus, shrinkage of the chloroplast, and appearance of viral particles during the lytic phase at 48 h postinfection (hpi), while no changes in cellular structure were observed in cells infected by the nonlytic EhV163 (Figures 1D to 1F). Accumulation of intracellular viral DNA started as early as 4 hpi in EhV201-infected cells and reached maximal values at 24 hpi (Figure 1G). This process preceded the release of viral particles, which reached their maximal extracellular level at 32 hpi (Figure 1H). This lytic infection pattern by EhV201 resembles the kinetics of coccolithovirus infection observed in natural populations (Pagarete et al., 2009; Vardi et al., 2012). Infection by the nonlytic EhV163 did not lead to induction of cell death or viral DNA replication (Figures 1C, 1G, and 1H). This unique experimental setup, in which a single host is infected either by lytic or nonlytic EhV, was further used to explore the molecular mechanisms underlying host–virus interactions.

Global Host-Virus Transcriptome Profiling

To gain a better understanding of the molecular mechanisms underlying the *E. huxleyi*–virus interaction, we performed an infection experiment for high-throughput transcriptomic analysis using RNA-seq technology to simultaneously detect alterations in host and virus gene expression profiles. Based on the observed viral infection dynamics (Figures 1A to 1H), RNA was extracted from cells infected with EhV201, EhV163, and from noninfected cells at 1 and 24 hpi and subjected to sequencing using an Illumina platform. In total, we sequenced around 410 million short reads of 100 bp from six libraries (Supplemental Data Set 1). Reads were aligned to viral genomes (Allen et al., 2006a; Nissimov et al., 2012), to an *E. huxleyi* transcriptome, which was constructed based on genomic data (Read et al., 2013), and a de novo transcriptome assembly (see Methods and Feldmesser et al., 2014). Gene expression normalization was performed independently to the host and viral genomes and transcript abundance estimation was performed using RSEM (Li and Dewey, 2011). A remarkable increase in viral RNA transcripts versus host transcripts was observed during lytic infection (Figure 1I). While at 1 hpi only 5% of the total reads where aligned with the EhV201 genome, at 24 hpi 80% of the total reads were aligned to the viral genome. Remarkable host transcriptome reprogramming was detected upon viral infection, whereby the expression level of the majority (30,658/42,385) of the *E. huxleyi* transcripts were attenuated during infection. Thus, lytic infection is accompanied by rapid remodeling of global gene expression.

Based on their expression pattern, we further clustered the host genes into 13 coexpressed groups using K-means (Figure 2A). Functional analysis of enriched biological terms was performed for each cluster using Gene Ontology (GO), Kyoto Encyclopedia of Genes and Genomes (KEGG), and Eukaryotic Orthologous Groups (KOG) (Figure 2B; Supplemental Data Set 2). For example, cluster 1 consists of host transcripts that are downregulated at 24 hpi during lytic infection (Figure 2A) and are enriched in photosynthetic genes (Figure 2B). This reduction in the photosynthetic machinery is in accord with ultrastructural changes in the chloroplast observed by TEM analysis (Figure 1E). In contrast, genes related to the pentose phosphate pathway and to nucleotide biosynthesis were significantly enriched in cluster 4, which exhibited moderate upregulation at 1 hpi and gradually increased at 24 hpi during lytic infection (Supplemental Figure 2). In addition, upregulation of pathways related to DNA damage, meiosis, and spermatogenesis were found during lytic infection (Clusters 7, 12, and 13, Figures 2A and 2B). These observations are in agreement with a previous

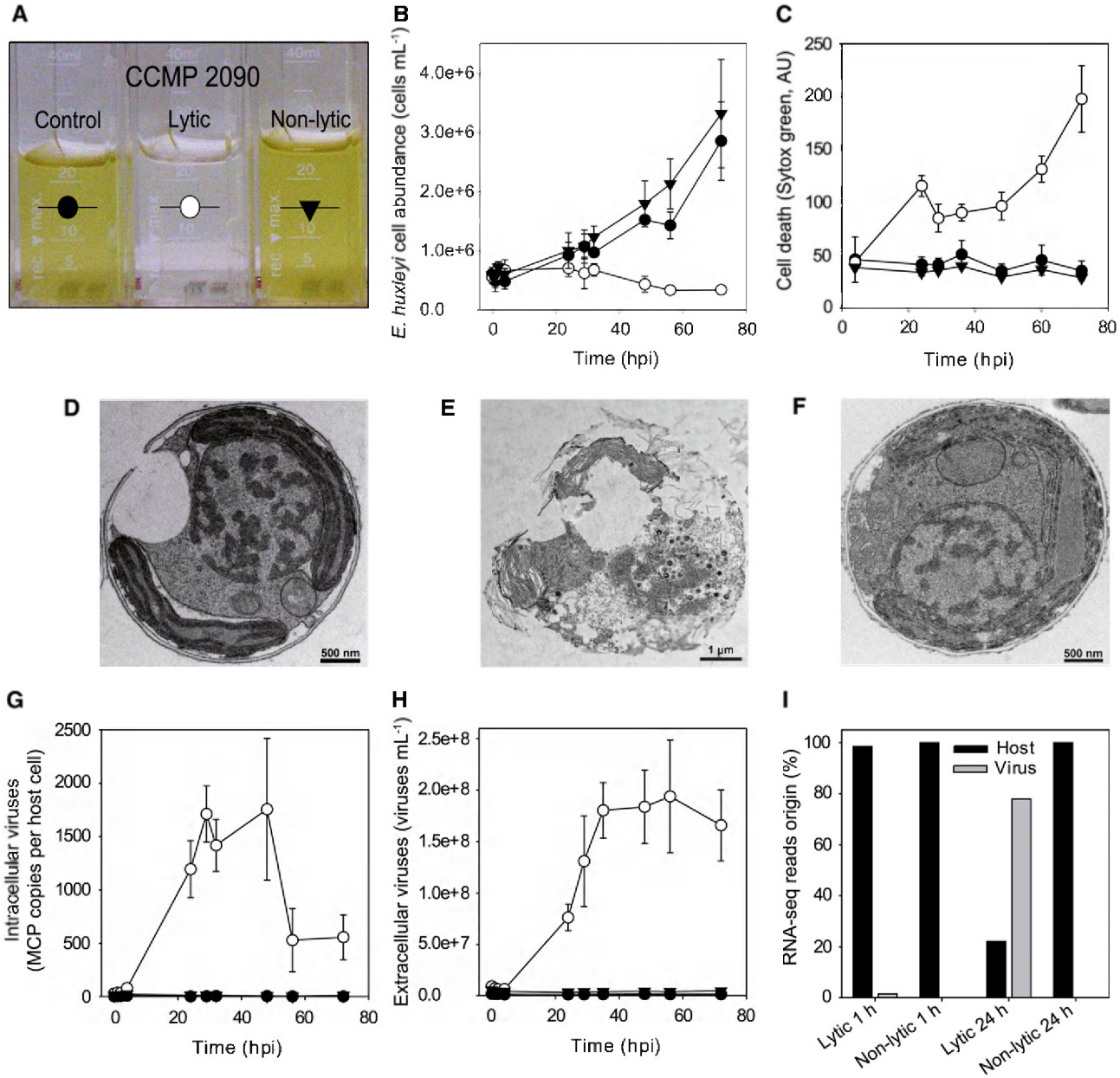

Figure 1. Infection Dynamics and Ultrastructure Analyses of *E. huxleyi* and Its Virus EhV.

(A) Cultures of *E. huxleyi* were monitored during infection by a lytic (EhV201) or nonlytic (EhV163) virus and compared with noninfected control cells. Images were taken at 72 hpi.

(B) and **(C)** Host cell abundance **(B)** and host cell death **(C)** as assessed by Sytox Green fluorescence by flow cytometry (mean ± SD, $n = 3$, at least 6000 cells were measured at each time point).

(D) to **(F)** Transmission electron micrographs of control cells **(D)** and cells infected by the lytic **(E)** and nonlytic **(F)** virus at 48 hpi. Viruses are only visible in lytic infected cells.

(G) Intracellular viral abundance determined by quantitative PCR of the viral DNA within the cellular fraction, probing the major capsid protein (MCP) gene (mean ± SD, $n = 3$).

(H) Abundance of extracellular viruses measured by flow cytometry (mean ± SD, $n = 3$).

(I) Relative abundance of RNA reads mapped to host or virus genomes at 1 and 24 hpi.

[See online article for color version of this figure.]

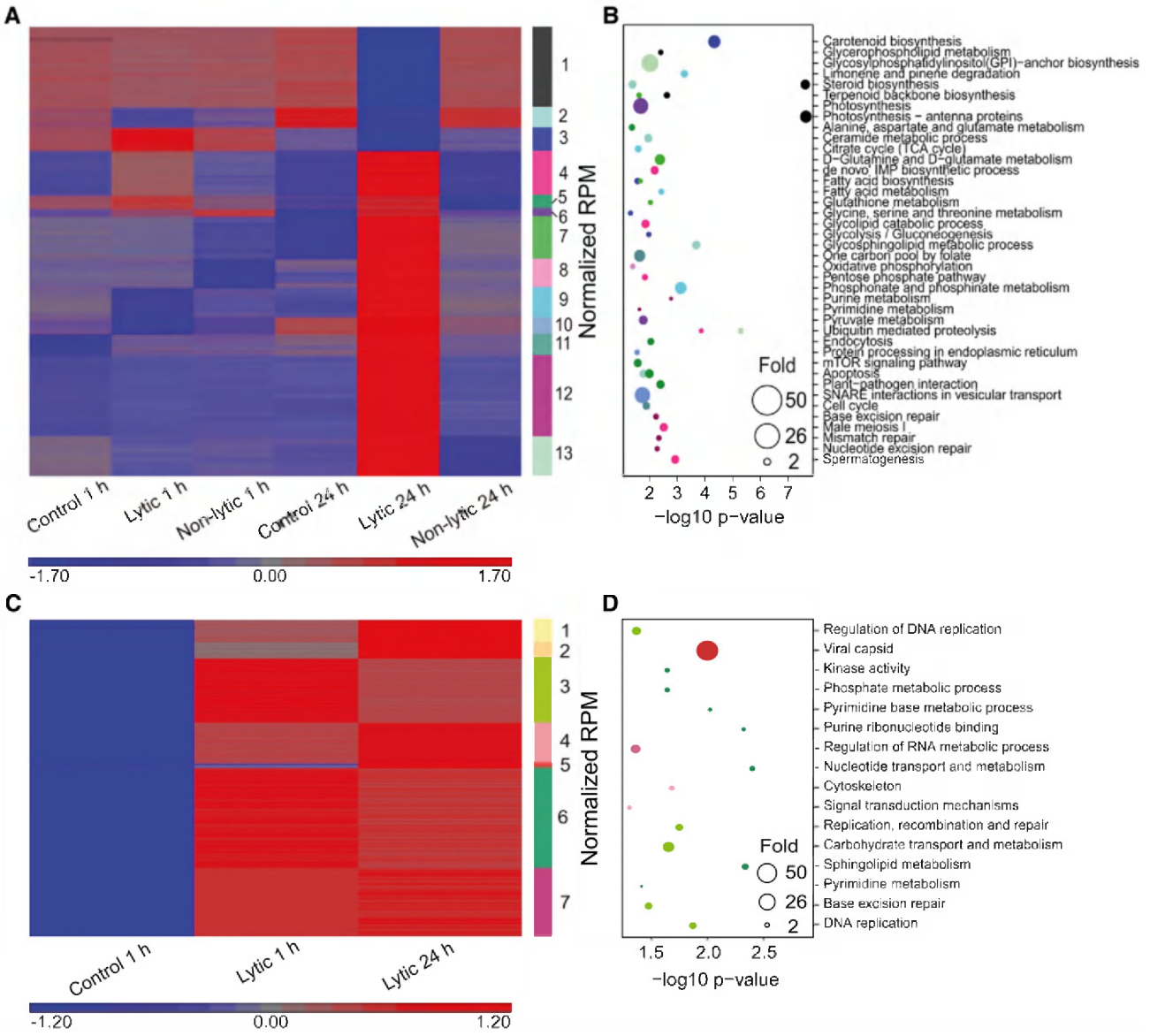

Figure 2. Global Gene Expression Profiles of *E. huxleyi* and EhV during Infection.

(A) Global gene expression profiles of host genes during infection by the lytic and nonlytic viruses. K-means clustering of genes with altered expression levels during the course of infection is presented. Red, high expression level; blue, low expression level.

(B) Significantly enriched GO terms and KEGG pathways (hypergeometric test, $P < 0.05$) related to host gene clusters as displayed in **(A)**. Colors refer to clusters as indicated in **(A)**. For a full list of enriched biological pathways in each cluster, see Supplemental Data Set 2.

(C) Global gene expression profiles of viral genes during lytic viral infection. K-means clustering of genes induced at the early and late phases of infection is shown. Red, high expression level; blue, low expression level.

(D) Significantly enriched biological functions (hypergeometric test, $P < 0.05$) related to viral gene clusters as displayed in **(C)**. Colors refer to clusters as indicated in **(C)**.

study that suggested a life cycle shift of *E. huxleyi* from the susceptible diploid to the resistant flagellated haploid life phase in response to viral infection (Frada et al., 2008). A significant upregulation was also found in glutathione metabolism genes at 24 hpi, suggesting the involvement of oxidative stress during lytic viral infection (Cluster 7, Figures 2A and 2B). Corroborating this data, ROS accumulation was found during EhV lytic infection in cultures (Evans et al., 2006) and in infected natural populations (Vardi et al., 2012).

Analysis of viral gene expression profiles revealed profound variation in viral expression at 1 hpi (Figure 2C), where highly transcribed regions can be detected in the viral genome (Supplemental Figure 3). High expression was detected in a genomic subregion between EhV218-366 (Supplemental Figure 3), a region that was

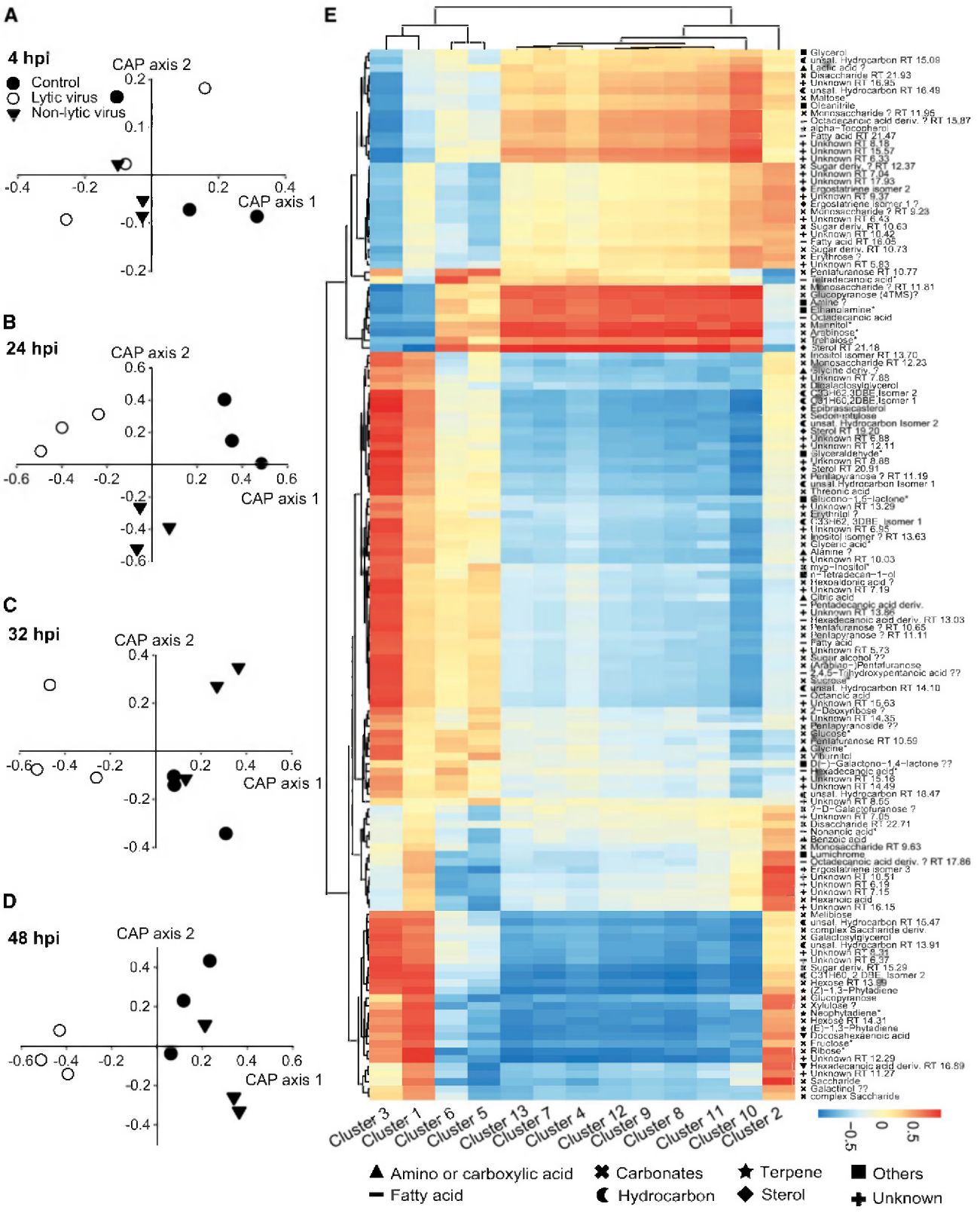

Figure 3. Viral-Induced Remodeling of Host Metabolism during Infection.

(A) to **(D)** CAP of metabolic profiles derived from control cells compared with cells infected by the lytic or nonlytic virus 4, 24, 32, and 48 hpi (n = 3). **(E)** Correlation of transcriptome expression patterns (1 and 24 hpi) and metabolite abundance (4 and 24 hpi) based on weighted correlation network analysis. Symbols indicate the affiliation of metabolites to metabolic classes. Blue, low correlation between transcriptome and metabolome; red, high correlation between transcriptome and metabolome. The numerical correlation coefficient values are given in Supplemental Data Set 7.

previously found to consist of early phase viral genes (Allen et al., 2006b). Among the most highly expressed viral genes at 1 hpi is deoxyuridine 5-triphosphate nucleotidohydrolase (EPVG_00218), which participates in nucleotide biosynthesis. As described for the host genes, clustering and functional analysis was performed for viral genes during lytic infection (Figures 2C and 2D). The gene encoding the major capsid protein was not expressed at 1 hpi and highly expressed at 24 hpi (viral cluster 5), while genes encoding enzyme involved in sphingolipid metabolism and the regulation of DNA replication were already induced at 1 hpi (Figures 2C and 2D; Supplemental Figure 3, see viral clusters 3 and 6).

Dynamic Modulation of Metabolism during Early Stages of Viral Infection

Our transcriptome analysis revealed alterations in numerous metabolic pathways, such as glycolysis, fatty acid, and nucleotide biosynthesis (Figure 2; Supplemental Figure 2). To determine global changes in host cell metabolism, we performed gas chromatography–mass spectrometry (GC-MS)–based metabolomics targeting central metabolism (Vidoudez and Pohnert, 2012) in parallel with transcriptome analysis. In total, we observed 185 signals at four time points (4, 24, 32, and 48 hpi) (see Supplemental Data Sets 3 and 4 for details). Nearly half of these (86 signals) were identified as specific metabolites by library comparison and/or coinjection with authentic standards. Forty-seven signals were tentatively assigned to a metabolite class based on their mass spectra, and 52 signals (~28.1%) remained unknown. Differential metabolomic analysis indicated profound rewiring of host metabolism during viral infection (Supplemental Data Set 4). We used canonical analysis of principal coordinates (CAP) (Anderson and Willis, 2003) to get a global overview of metabolic differences between the treatments. Cells infected by lytic EhV201 or nonlytic EhV163 and control cells were assigned as groups and each time point was analyzed separately. At 4 hpi, treatments showed no statistical separation (permutation test $P = 0.7275$) (Figure 3A); accordingly, axes were not differentiating between groups (Supplemental Data Set 5). However, as viral infection progressed, metabolic profiles of all treatments at all later time points were resolved statistically (permutation test 24 hpi, $P = 0.0058$; 32 hpi, $P = 0.0215$; and 48 hpi, $P = 0.01$) (Figures 3B to 3D) and supported by CAP diagnostic values (Supplemental Data Set 5). These correlation patterns were driven by discriminating metabolites that were specific for each time point (Supplemental Data Set 6). Interestingly, infection with the nonlytic virus resulted in a temporal separation of metabolic profiles, as at 24 hpi this group showed higher similarity to the lytic group but subsequently resembled the control (Figures 3C and 3D) (confirmed by cross-validation). This trend suggested a critical phase of metabolite production impaired in the nonlytic infection. In contrast, the three biological replicates of the lytic infection were well separated from the other groups. This analysis shows profound alterations in cellular metabolism during lytic and nonlytic infection.

Joint Transcriptome and Metabolome Data Analysis

We used weighted correlation network analysis (Langfelder and Horvath, 2008) to correlate gene cluster profiles to levels of metabolites measured under the same timing and type of viral infection. Since transcriptome data from 1 hpi were reflected in the metabolome at 4 hpi, these sets were combined for the early time point in the analysis. Many of the identified metabolites were highly correlated to the expression pattern of host cluster 3 (Figures 2A and 3E; Supplemental Data Set 7 and Supplemental Figure 4). During lytic infection, this specific cluster exhibited upregulation during early infection and downregulation at 24 hpi, whereas in nonlytic infection, a moderate upregulation was evident at the onset of infection (Figures 2A and 4B). Indeed, functional analysis of cluster 3 revealed enrichment of biological functions related to metabolism, including glycolysis, fatty acid, and amino acid biosynthesis (e.g., alanine, glutamate, glycine, and serine metabolism) (Figure 2B). Figure 4A presents an integrated metabolic map of these pathways, highlighting corresponding enzymes and the abundance of several associated metabolites.

Upregulation of Glycolytic Enzymes during Early Viral Infection

Almost all glycolytic enzymes participating in pyruvate production from glucose were clustered together and exhibited upregulation at 1 hpi followed by downregulation at 24 hpi in lytic infected cells. In accordance, glucose levels showed higher concentrations in infected cells as compared with control cells at all time points, suggesting a breakdown of macromolecules such as glycolipids and storage carbohydrates, which supports glycolytic activity. In addition, a moderate increase in glucose was also observed in nonlytic infected cells (fold change >1.0 to 1.4). Nonphosphorylated forms of glycolysis products such as fructose, glyceraldehyde, and glyceric acid were all more abundant at 4 hpi in cells infected by the lytic virus, with the most pronounced increase in glyceric acid (4.1-fold). At later time points, these metabolites showed decreased concentrations in comparison to noninfected cells, suggesting their rapid consumption by downstream metabolic reactions. In cells infected by the nonlytic virus, fructose and glyceric acid were generally more abundant, whereas glyceraldehyde was slightly decreased at 24 and 32 hpi (fold change <1.0 and 0.7, respectively) (Figure 4; Supplemental Data Set 4). Taken together, these observations indicate the upregulation of host glycolysis during the early phases of viral infection.

De Novo Fatty Acid Biosynthesis Is Crucial for Viral Production

Expression patterns of genes related to fatty acid biosynthesis were strongly affected by lytic viral infection. The pyruvate dehydrogenase transcript was also found in cluster 3 and exhibited upregulation at 1 hpi (Figures 4A and 4B). This enzyme catalyzes the production of acetyl-CoA from pyruvate, which may then feed into the tricarboxylic acid (TCA) cycle. Interestingly, the only TCA cycle enzyme belonging to cluster 3 is citrate synthase, which catalyzes the formation of citrate from acetyl-CoA and oxaloacetate. This suggests that the upregulation of glycolysis feeds the "citrate shuttle," which transports a portion of the mitochondrial pool of acetyl-CoA to the cytosol. In agreement, the metabolic level of citrate was significantly elevated in lytic infected cells at 4 hpi (9.1-fold) and decreased afterwards (Figure 4A). A milder induction (fold change >2.3) was also detected during nonlytic infection. Higher concentrations of citrate can feed fatty acid

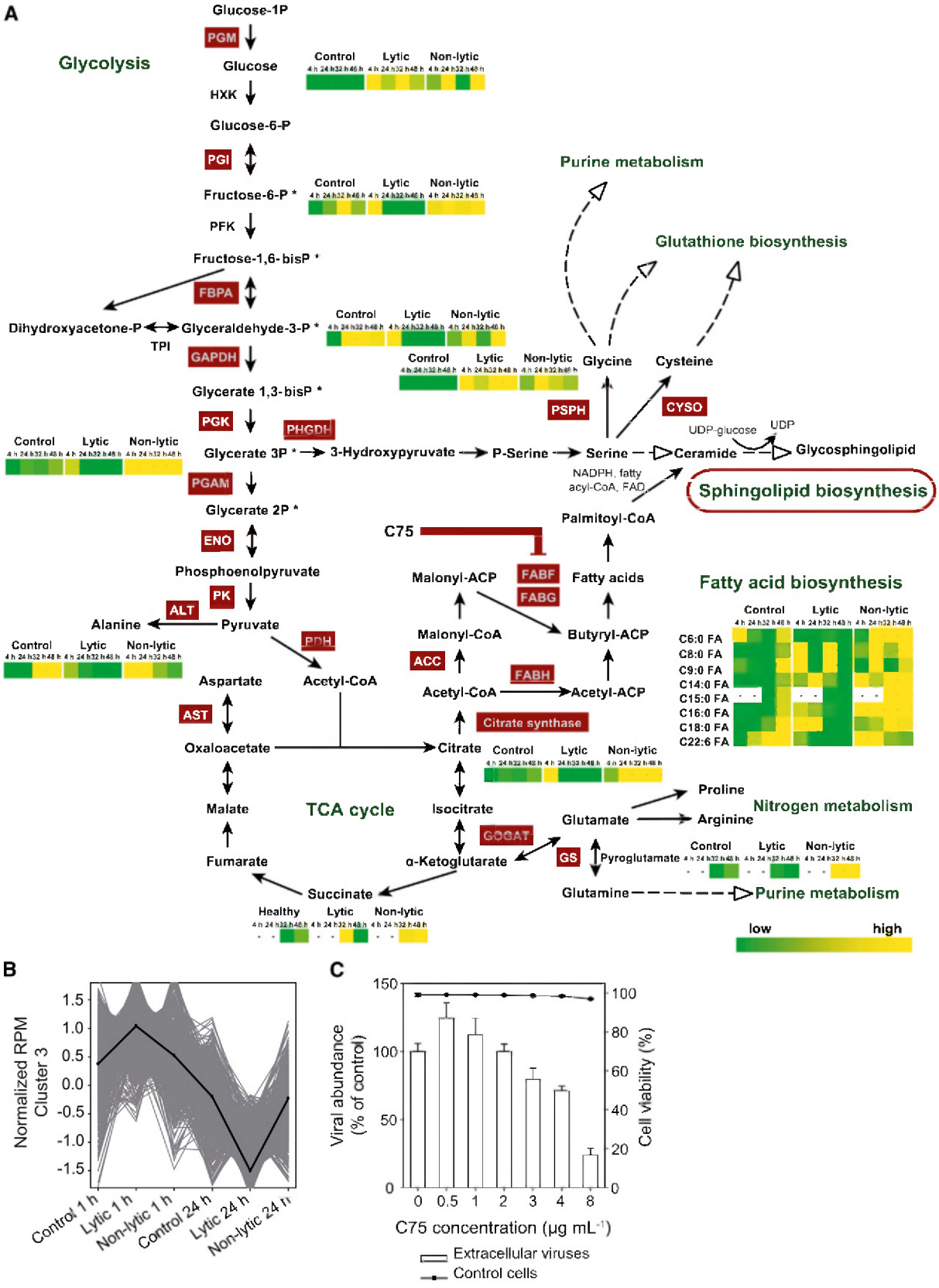

Figure 4. Viral-Induced Rewiring of Host Metabolism Leads to an Increase in Fatty Acid Biosynthesis.

biosynthesis; indeed, the expression of key genes of this process, such as the rate-limiting enzyme acetyl-CoA carboxylase and fatty acid synthase (FAS), were upregulated (Figure 4A). In cells infected by the lytic virus, most free fatty acids (C8-C16) showed higher concentrations at 4 and 32 hpi (fold change 1.1 to 2.4) relative to control cells, whereas long-chain fatty acids (C18 and C22:6) decreased at 32 hpi (docosahexaenoic acid, already at 24 hpi) (Figure 4A; Supplemental Data Set 4). In contrast, nonlytic infected cells displayed higher concentrations of fatty acids at almost all time points, with a slight reduction in docosahexaenoic acid at 32 and 48 hpi when compared with control cells. These results suggest the upregulation of fatty acid biosynthesis at the early phases of viral infection. Accumulation of fatty acids during the nonlytic infection might be due to their overproduction without consumption in the process of viral assembly.

Treatment of *E. huxleyi* cells with the FAS inhibitor C75 (4-methylene-2-octyl-5-oxotetrahydrofuran-3-carboxylic acid) resulted in a dose-dependent reduction in extracellular viral production (Figure 4C). Interestingly, the amount of intracellular viral DNA production was not reduced by the inhibitor (Supplemental Figure 5). C75 concentrations that inhibited viral production were not toxic for *E. huxleyi* cells, as >90% of the cells were viable (Figure 4C; Supplemental Figure 5). Taken together, these results demonstrated the pivotal role of fatty acid biosynthesis in EhV assembly and egress.

A Metabolic Shift toward Viral Sphingolipids during Infection

Genome analysis of EhV revealed a suite of putative genes involved in de novo sphingolipid biosynthesis. The RNA-seq–based transcriptome profiling allowed us to simultaneously monitor and compare expression patterns in host and virus genes encoding central enzymes in sphingolipid biosynthesis. Host genes encoding enzymes involved in sphingolipid metabolism were enriched in cluster 2, which exhibited downregulation at 1 hpi (Figures 2A and 2B). On the contrary, viral sphingolipid biosynthetic genes were enriched in viral cluster 6, which consists of early-induced genes (Figures 2C and 2D), suggesting shutdown of host sphingolipid metabolism and upregulation of the viral enzymes related to sphingolipids. We mapped the sphingolipid pathways and annotated related genes in the host and viral genomes. A detailed analysis of gene expression profiles, based on the transcriptomics and quantitative PCR data, of both host- and virus-derived sphingolipid metabolism revealed a profound overexpression of viral genes participating in de novo sphingolipid biosynthesis, such as serine palmitoyltransferase (SPT), dihydroceramide desaturase (DCD), and ceramide synthase (CerS), at the early stages of infection. In contrast, host homologous genes were downregulated at 1 and 24 hpi during lytic infection (Figure 5A; Supplemental Figure 6 and Supplemental Data Set 8). In agreement, using liquid chromatography–mass spectrometry–based analysis, we detected a strong induction of viral-specific glycosphingolipid (vGSL) only during the lytic infection. vGSL levels were induced as early as 4 hpi in lytic-infected cells (fold change 6.3) and peaked at 32 hpi (fold change 76) in comparison to nonlytic infection (Figure 5B). In contrast to the vGSL induction, the levels of two host glycosphingolipids (hGSL and sGSL) were not significantly changed during the infection (Figure 5B). Interestingly, we observed upregulation of host genes encoding catabolic enzymes of complex sphingolipids such as ceramidase, sphingosine kinase (SPHK1), and glucocerebrosidase (GBA) (Figure 5A; Supplemental Figure 6 and Supplemental Data Set 8). Concomitantly, we found downregulation of host UDP-glucose ceramide glucosyltransferase (UGCG), which catalyzes sphingolipid glycosylation. As both host and viral enzymes may compete for the same substrates, these results suggest that the host de novo sphingolipid machinery is shut down during lytic infection together with extensive viral-induced machinery to synthesize unique viral sphingolipids.

Specific Inhibition of Isoprenoid Biosynthesis Reduces Viral Assembly and Production

Metabolomic analysis indicated that several terpenes, including sterols, were severely reduced in concentration exclusively during lytic infection (Figure 6A; Supplemental Data Set 4). This metabolic pattern was well corroborated with transcriptomics data (Figure 3E), in which we also found a profound downregulation in expression patterns of genes encoding enzymes involved in terpenoid biosynthesis at 24 hpi (host cluster 1, Figures 2A and 2B). We detected downregulation of all host genes related to the production of isopentenyl-pyrophosphate from acetyl-CoA in the mevalonate (MVA) pathway (Figures 6A and 6B). Furthermore, two genes encoding enzymes of the methylerythritol phosphate (MEP) pathway were downregulated (Figures 6A and 6B). Accordingly, during late lytic infection (32 and 48 hpi), levels of diterpenoids, including phytol, neophytadiene, and two phytadiene isomers, strongly decreased (Figure 6A; Supplemental Data Set 4). Sterols, among which we found epibrassicasterol, three putative isomers

Figure 4. (continued).

(A) Integrated metabolic map of significantly enriched biological pathways in host gene cluster 3. Genes associated with cluster 3 are marked in dark red. Inserted heat maps present normalized intensities (mean, $n = 3$) of specific metabolites in noninfected *E. huxleyi* cells and cells infected by the lytic or nonlytic virus at 4, 24, 32, and 48 hpi. Dark-red bar indicates inhibition of fatty acid biosynthesis by C75. Fold-change values of changes in metabolite concentration relative to the control are presented as Supplemental Data Set 4. Metabolites marked by an asterisk were detected in nonphosphorylated form and a minus sign indicates the absence of a metabolite at a specific time point. Dashed lines refer to connections via a known metabolic pathway. Green, low metabolite concentration; yellow, high metabolite concentration. For abbreviations of enzyme names, see Supplemental Data Set 12.
(B) Gene expression pattern of host cluster 3. The average of the expression normalized values is presented as thick black line.
(C) The effect of inhibition of fatty acid biosynthesis by various concentrations of C75 on extracellular virus abundance at 72 hpi relative to viruses released from infected cells without the addition of the inhibitor (percentage of control) (mean ± SD, $n = 3$), and the percentage of viable cells at 24 hpi as measured by flow cytometry (mean ± 3·SD, $n = 3$). FA, fatty acid; P, phosphate; RPM, reads per million.

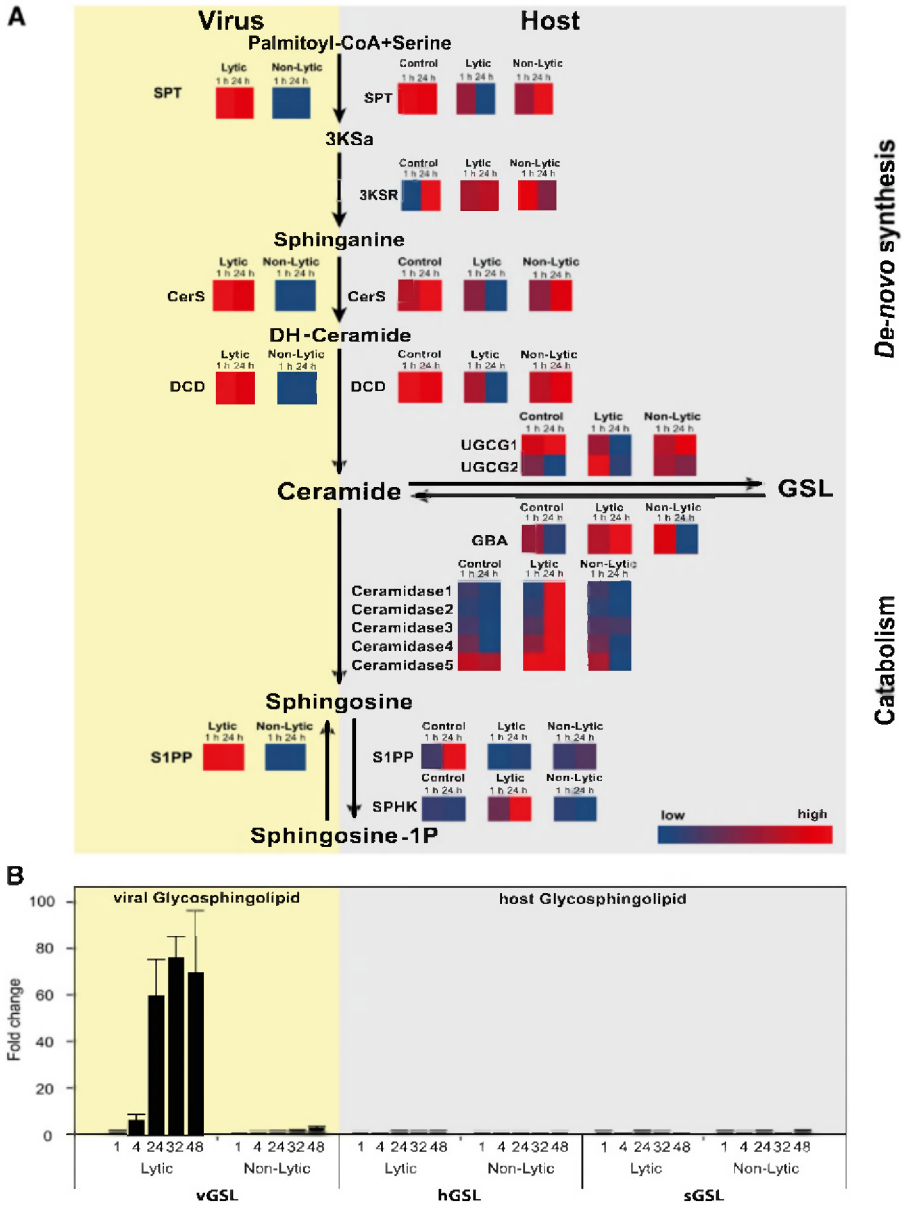

Figure 5. Sphingolipid Metabolic Network Is Modulated toward Production of Viral-Derived Sphingolipids during Lytic Infection.

(A) RNA-seq–based gene expression profiles of host (gray) and viral (yellow) genes encoding enzymes in sphingolipid metabolism during infection with the lytic or nonlytic virus at 1 and 24 hpi. Host de novo synthesis (top) and catabolic reactions (bottom) are indicated. Blue, low relative expression; red, high relative expression. Reads per million (RPM) values for the associated genes are presented as Supplemental Data Set 8.

(B) Relative abundance of vGSL and two host glycosphingolipids (hGSL and sGSL) are shown at 1, 4, 24, 32, and 48 hpi. vGSL relative abundance was normalized to its level in the nonlytic infection at 1 hpi and was not detected in control cells. Host sphingolipid abundance was normalized to noninfected cells. For abbreviations of enzyme names, see Supplemental Data Set 12. 3KSa, 3-ketosphinganine; DH, dihydro; GSL, glycosphingolipid; hGSL, host glycosphingolipids; P, phosphate; sGSL, sialic acid glycosphingolipids. Data are presented as mean ± SE; $n = 3$.

of $\Delta^{5,22}$ ergostatriene (sterols 1 to 3) and probably ergostadienone (sterol 4), showed a similar profound depletion during lytic infection (Figure 6A; Supplemental Data Set 4). In cells infected by the nonlytic virus, terpenes and sterols mostly displayed concentrations similar or weakly increased compared with control cells.

We applied specific inhibitors of the different branches of terpenoid biosynthesis and examined their effect on viral productivity. Pretreatment of *E. huxleyi* cells with cerivastatin, a specific inhibitor of 3-hydroxy-3-methylglutaryl-CoA reductase in the MVA pathway (Mason, 2006), prior to viral infection resulted in a reduction in extracellular viral production (Figure 6C). In contrast, application of fosmidomycin, which specifically inhibits 1-deoxy-D-xylulose-5-phosphate reductoisomerase (Yeh and DeRisi, 2011), an enzyme involved in the MEP route, did not affect viral productivity at any of

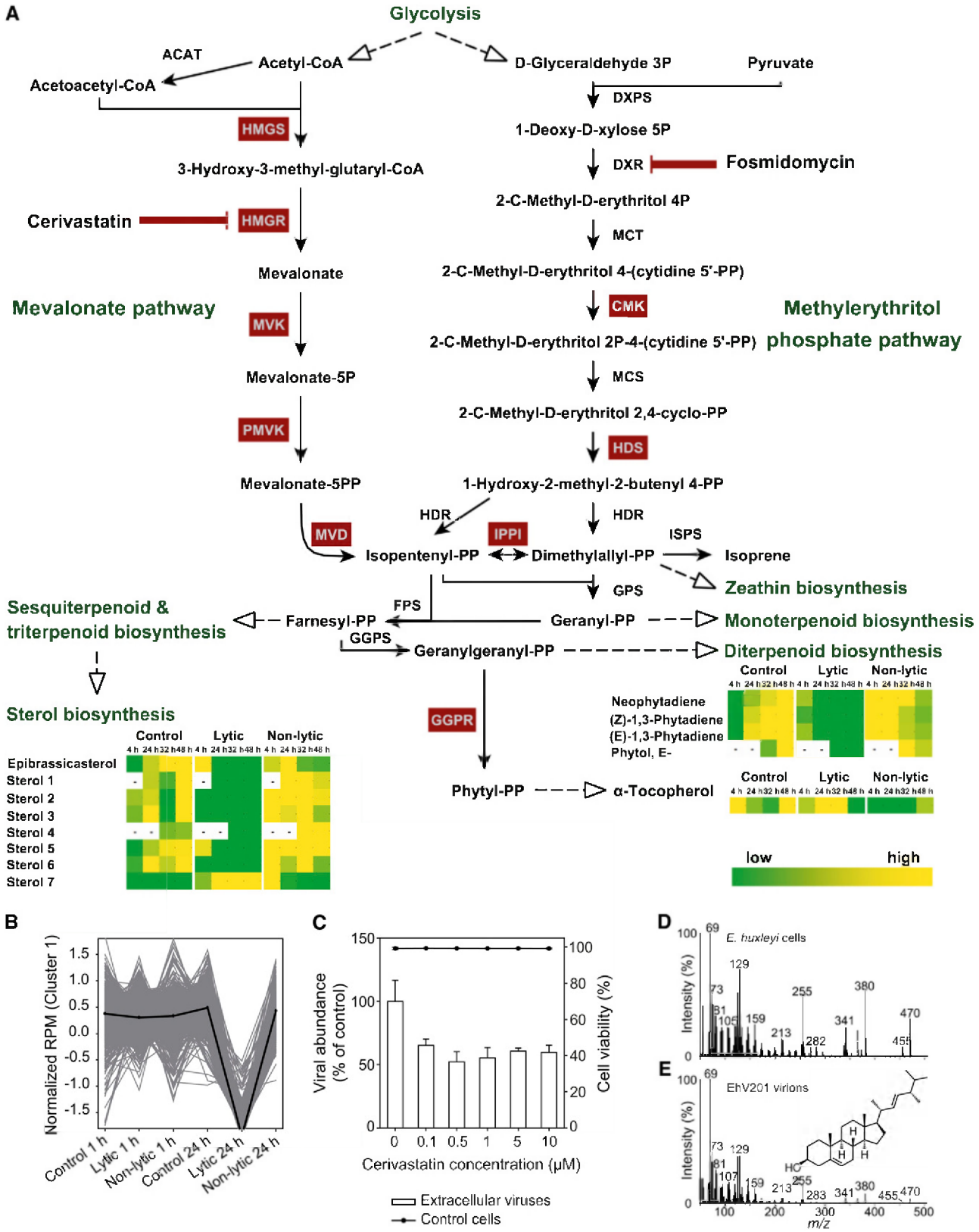

Figure 6. Terpenoid and Sterol Biosynthesis via the Mevalonate Pathway Is Required for Viral Replication.

the concentrations tested (Supplemental Figure 7). Interestingly, the level of intracellular viral DNA production was not significantly affected by cerivastatin (Supplemental Figure 8). In addition, neither of the inhibitors was toxic to *E. huxleyi* cells (>95% viable cells) (Figure 6C; Supplemental Figures 7 and 8). Taken together, these observations indicate the MVA branch in terpenoid biosynthesis as an essential component of the viral replication cycle.

We further hypothesized that the observed depletion of sterols is due to their consumption by the released viruses. In this scenario, downregulation of terpenoid biosynthesis may serve as an antiviral strategy by limiting viral resources. To further test this hypothesis, we analyzed the metabolic profile of isolated EhV201 virions (Supplemental Data Set 9). Interestingly, we detected (24*S*)-24-methylcholesta-5,22*E*-diene-3β-ol, epibrassicasterol, which is the dominant sterol of the host (Figure 6D) in isolated purified virions (Figure 6F), suggesting it is a constituent of the viral membranes.

DISCUSSION

We applied transcriptomic, metabolomic, and pharmacologic approaches to reveal the central role of viral-induced alterations in cellular metabolism during the interaction between the coccolithophore *E. huxleyi* and its specific viruses. The comparative study between lytic and nonlytic viral infection strategies induced within the same host allowed deciphering of key cellular processes specific for host responses to lytic viral replication. We identified biochemical pathways that mediate key metabolic switches during infection by a large dsDNA virus. We could further link rapid transcriptomic reprogramming, within 1 h of lytic infection, to its subsequent manifestation in metabolic changes within infected *E. huxleyi* cells.

Based on transcriptomic profiling, we predicted an increase in the glycolysis flux toward de novo biosynthesis of fatty acids in the lytic infection. This was supported by elevated C8-C16 fatty acid levels in the early stages of lytic infection (Figure 4). These data are in accord with an increase in saturated fatty acids (Evans et al., 2009) and upregulation of genes encoding for glycolysis and lipid metabolism during infection of *E. huxleyi* cells (Kegel et al., 2010; Pagarete et al., 2011). The dependence of viral production on this metabolic shift toward fatty acids was supported by the reduction in viral release caused by inhibition of de novo fatty acid synthesis (Figure 3). In contrast to small RNA plant viruses, large dsDNA viruses infecting algae have large metabolic demands, which need to be met by their hosts. With an average burst size of 500 viruses/cell (Bratbak et al., 1993) and estimates of 0.15 to 0.35 fg lipids/virion (Vardi et al., 2009), a single cell will have to turn over or de novo produce 60 to 180 fg of lipids per host cell during infection. These results are also in agreement with several reports that describe the dependence of human viruses on host fatty acid metabolism. Human cytomegalovirus upregulates central carbon metabolism, including glycolysis (Munger et al., 2008), shuffling energy toward fatty acid biosynthesis (Vastag et al., 2011). Upregulation of these pathways, together with induction of the pentose phosphate pathway and amino acid production, were also detected during infection of human endothelial cells by Kaposi's Sarcoma-associated Herpes virus (Delgado et al., 2012). The similarity of strategies used by these evolutionarily distant viruses to hijack host metabolic pathways suggests this metabolic remodeling as a conserved viral mechanism.

Our metabolomic and transcriptomic analyses revealed a nearly complete shutdown of terpenoid biosynthesis pathways as lytic infection proceeded (Figure 7), a hitherto unrecognized metabolic pathway in the context of host-pathogen interactions at sea. Two major pathways for terpenoid biosynthesis are encoded in the *E. huxleyi* genome, the cytosolic MVA and the plastidic MEP pathway (Read et al., 2013). We found that specific inhibition of the MVA pathway led to a reduction in released viruses. These data clearly indicated that specific products of this metabolic branch are needed for viral production (Figure 6). Triterpenoids are the building blocks for sterols, which in algae are derived from the MVA pathway (Disch et al., 1998). These molecules constitute parts of cellular membranes (Hartmann, 1998), including viral envelopes (Selstam and Jackson, 1983). Therefore, the reduction in sterol abundance during viral infection can be a result of its consumption by newly produced viruses. Indeed, we detected epibrassicasterol, the dominant sterol in *E. huxleyi* (Maxwell et al., 1980) and derived from the MVA pathway (Disch et al., 1998), in isolated purified EhV virions (Figures 6D and 6E). West Nile Virus can also modulate host cell cholesterol homeostasis by upregulating cholesterol biosynthesis and redistributing cholesterol to

Figure 6. (continued).

(A) Enzymatic and metabolic patterns of terpenoid and sterol biosynthesis as comprised in host gene cluster 1. Genes associated with cluster 1 are marked in dark red. Inserted heat maps present normalized intensities (mean, $n = 3$) of specific metabolites in *E. huxleyi* control cells and cells infected by the lytic or nonlytic virus at 4, 24, 32, and 48 hpi. Dark-red bars indicate inhibition of the MVA pathway by cerivastatin and of the MEP pathway by fosmidomycin. Sterols 1 to 3 are isomers of ergostatriene, sterol 4 is a putative ergostadienone, and sterols 5 to 7 remain unidentified. Dashed lines refer to connections via a known metabolic pathway. A minus sign indicates the absence of a metabolite at a specific time point. Green, low metabolite concentration; yellow, high metabolite concentration. Fold-change values of changes in metabolite concentration relative to the control are presented in Supplemental Data Set 4. For abbreviations of enzyme names, see Supplemental Data Set 12.

(B) Gene expression pattern of host cluster 1. The average of the expression normalized values is presented as a thick black line.

(C) The effect of inhibition of the MVA pathway by cerivastatin on extracellular virus abundance at 72 hpi relative to viruses released from infected cells without the addition of the inhibitor (percentage of control) (mean ± SD, $n = 3$) and the percentage of viable cells at 24 hpi as measured by flow cytometry (mean ± 3·SD, $n = 3$).

(D) Mass spectrum of epibrassicasterol, the main sterol in *E. huxleyi* cells.

(E) Mass spectrum of epibrassicasterol isolated from concentrated, purified EhV201 virion membranes. The insert displays the structure of the compound. P, phosphate; PP, pyrophosphate; RPM, reads per million.

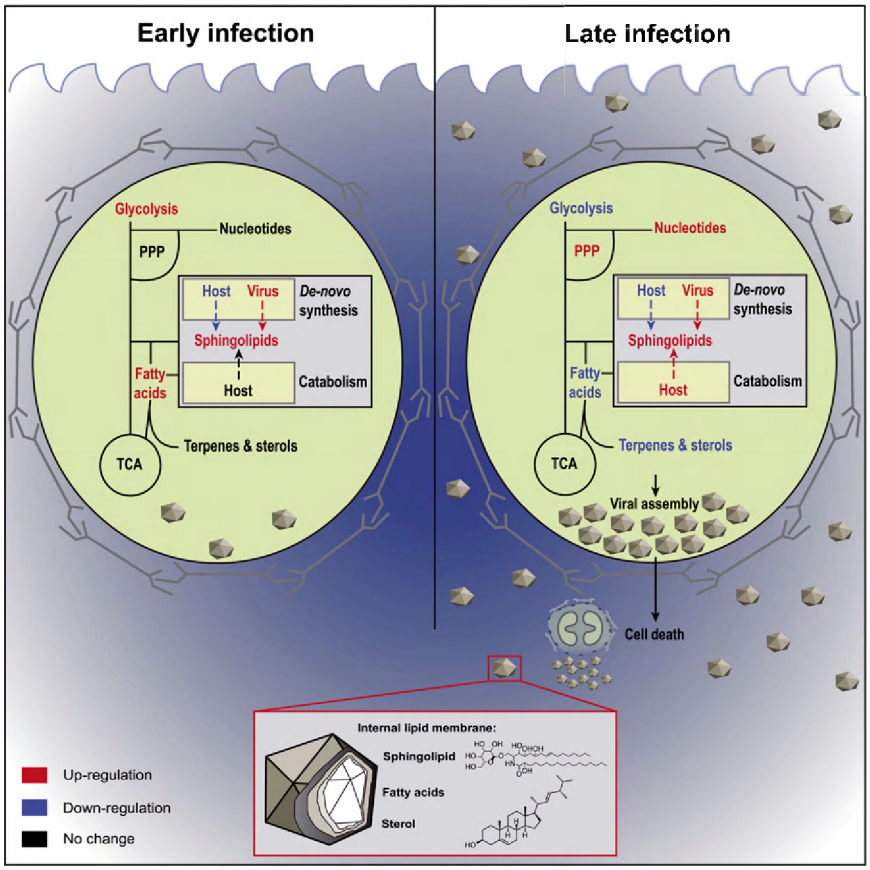

Figure 7. Rewiring of Host Metabolism during Lytic Viral Infection.

Viral replication in *E. huxleyi* depends on the host metabolic machinery to provide building blocks for viral progeny formation (e.g., sphingolipids, fatty acids, and sterols in the lipid membrane). During the early stage of viral infection, upregulated glycolysis shuffles energy to fatty acid biosynthesis, bypassing the TCA. Concomitantly, overexpression of viral encoded sphingolipid genes induces de novo sphingolipid biosynthesis. During the onset of lytic infection demands for nucleotide biosynthesis are met via upregulation of the pentose phosphate pathway (PPP). These processes result in assembly of progeny viruses and finally lead to host cell death. (Inset: graph of virion based on Hurst [2011]). Downregulation of fatty acid, terpenoid, and sterol biosynthesis in addition to induction of host-derived sphingolipid catabolic reactions in the late phase of viral infection may facilitate host resistance responses.

viral replication membranes (Mackenzie et al., 2007). The detection of sterol in viral membranes along with the specific role of the MVA pathway solely in lytic infection demonstrated how critical host-derived terpenoid metabolism is for viral production and release (Figure 6). Reduction of cholesterol biosynthesis at both the transcriptional and metabolic level, regulated by an interferon regulatory loop mechanism, was recently reported as an antiviral defense strategy of bone marrow-derived cells infected by human cytomegalovirus (Blanc et al., 2011). Another terpenoid-based regulation of viral replication is posttranslational prenylation of viral proteins. The role of a geranylgeranylated protein in integrating newly synthesized proteins into virions has been shown in Murine leukemia virus (Overmeyer and Maltese, 1992) and in RNA replication of hepatitis C virus (Ye et al., 2003; Kapadia and Chisari, 2005). Our data demonstrated downregulation of genes encoding enzymes of the MVA pathway at 24 hpi, pointing at a possible similar regulation mechanism. Future studies will investigate if isoprenylation plays similar roles in regulating viral proteins during EhV infection.

Unlike fatty acid and terpenoid metabolism, where the viral requirements are solely dependent on the host metabolic network, the production of sphingolipids is facilitated by viral genes that encode de novo sphingolipid enzymes. We detected profound upregulation of these viral genes upon infection, in stark contrast to the simultaneous downregulation of the homologous host sphingolipid genes (Figure 7), demonstrating a metabolic shift from host- to viral-specific sphingolipid production. In vitro studies showed that the EhV-encoded SPT preferentially utilizes myristoyl-CoA as a substrate, rather than the classical host SPT that uses palmitoyl-CoA (Han et al., 2006). Indeed, production of viral-derived sphingolipids (e.g., vGSL) was recently demonstrated and suggested to have a functional role in viral assembly as they are major constituents of viral membranes (Vardi et al., 2009, 2012; Fulton et al., 2014). Our metabolome analysis clearly indicated increased levels of fatty acids, amino acids, and glucose.

The last provides an essential head-group for the massive requirement of viral glucosyl ceramides (e.g., vGSL). Specific fingerprinting of viral-derived sphingolipids revealed a unique signature of multihydroxylated C16-based long-chain base forms in infected cultures and natural populations (Vardi et al., 2012; Fulton et al., 2014).

While host genes encoding enzymes involved in the de novo synthesis of sphingolipids were downregulated as early as 1 hpi, coinciding with the large upregulation of viral genes, host genes responsible for recycling of sphingolipids (salvage pathway) were upregulated at 24 hpi during lytic infection (Figures 5 and 7). The upregulation of genes encoding enzymes participating in the recycling of different species of sphingolipids as glycosphingolipids (e.g., GBA), ceramides (e.g., ceramidases), and sphingosines (e.g., sphingosine kinase) can support viral requirements for unique substrates to produce bioactive viral sphingolipids. Alternatively, upregulation of host genes for sphingolipid catabolism can serve as an antiviral strategy to prevent the accumulation of viral sphingolipids. The downregulation of UGCG, which is encoded exclusively by the host and catalyzes ceramide glycosylation, thus may act as an antiviral strategy to inhibit the biosynthesis of vGSL that is enriched in EhV viral membranes (Vardi et al., 2009).

Ceramides are known signaling lipids that can induce PCD in plants (Liang et al., 2003) and mammals (Mullen and Obeid, 2012). Therefore, an extensive upregulation of five host ceramidase genes after the onset of lytic infection (Figure 5) could potentially serve as a viral strategy to inhibit host-induced cell death by breakdown of toxic ceramides to sphingosines. In this view, upregulation of sphingosine kinase (SphK), which produces sphingosine-1-phosphate from sphingosine, a conserved signaling lipid involved in diverse cellular responses in mammals (Spiegel and Milstien, 2003), can serve as a host strategy to induce antiviral signaling pathways. Despite the importance of sphingolipids in programmed cell death, the molecular mechanism that mediates the interplay between sphingolipid signaling and PCD has yet to be identified (Berkey et al., 2012). Recently, the role of sphingolipid metabolism in the mitochondria during apoptosis mediated by BAK/BAX activation was demonstrated (Chipuk et al., 2012). Little is known about the molecular components involved in executing PCD in photosynthetic microorganisms, as the classical animal apoptotic components, such as the Bcl-2 protein family, p53, and caspases, are lacking from their genomes. Therefore, further investigations into the molecular mechanism underlying sphingolipid-induced cell death under viral infection are essential and may also provide insight into the unexplored PCD pathway of unicellular organisms.

The recent accumulation of genomic information from marine viruses brought to light several intriguing examples of viral genomes carrying auxiliary metabolic genes (Hurwitz et al., 2013; Enav et al., 2014). These enable viral strategies to manipulate host metabolic networks and include genes involved in photosynthesis (Lindell et al., 2005; Sharon et al., 2009), the pentose phosphate pathway (Thompson et al., 2011), phosphate regulation (Zeng and Chisholm, 2012), polysaccharide synthesis (DeAngelis et al., 1997), and DNA and RNA processing (Yutin and Koonin, 2009; Arslan et al., 2011). The unique example of EhV is fascinating, as an almost complete metabolic network for sphingolipid metabolism is encoded by the virus (Monier et al., 2009). The high prevalence of viral-encoded metabolic enzymes in aquatic systems strongly points at their central role in shaping the evolutionary chemical "arms race" among marine microbes.

METHODS

Culture Growth and Viral Infection Dynamics

Cells of the noncalcifying *Emiliania huxleyi* strain CCMP2090 were cultured in k/2 medium (Keller et al., 1987) and incubated at 18°C with a 16:8 h light/dark illumination cycle. A light intensity of 100 μM photons·m^{-2}·s^{-1} was provided by cool white fluorescent lights. All experiments were performed with exponential phase cultures ($5 \cdot 10^5$ to 10^6 cells·mL^{-1}). Viruses used for this study are *E. huxleyi* virus EhV201 (lytic) and EhV163 (nonlytic) (Schroeder et al., 2002). In all infection experiments, *E. huxleyi* was infected with a 1:50 volumetric ratio of viral lysate to culture (multiplicity of infection of ~1:1 viral particles per cell).

Inhibition of Fatty Acid and Terpene Biosynthesis

For FAS inhibition experiments, methylene-2-octyl-5-oxotetrahydrofuran-3-carboxylic acid (C75) in DMSO (5 mg mL^{-1}) was added to cultures directly before infection with EhV201 to reach a final concentration of 0, 0.5, 1, 2, 3, 4, and 8 μg mL^{-1}. An equal volume of DMSO was added to all control cultures. For inhibition of terpenoid biosynthesis, fosmidomycin, which inhibits 1-deoxy-D-xylulose-5-phosphate reductoisomerase, or cerivastatin, which inhibits 3-hydroxy-3-methylglutaryl-CoA reductase (5 mg mL^{-1} dissolved in water), was added to cultures 2 h before infection with EhV201, to reach a final concentration of 0, 0.1, 0.5, 1, 5, and 10 μM. Culture conditions were identical to those described above.

Enumeration of Cell and Virus Abundance

Cells were monitored and quantified using an Eclipse (iCyt) flow cytometer, equipped with 405- and 488-nm solid state air-cooled lasers (both 25 mW on the flow cell) and standard filter setup. Algae were identified by plotting chlorophyll fluorescence in the red channel (737 to 663 nm) versus green fluorescence (500 to 550 nm) or side scatter. For extracellular viral production, samples were filtered using 0.45 μM polyvinylidene fluoride filters (Millex-HV; Millipore). Filtrate was fixed with a final concentration of 0.5% glutaraldehyde for 30 min at 4°C, plunged into liquid nitrogen, and stored at −80°C until analysis. After thawing, 2:75 ratio of fixed sample was stained with SYBER gold (Invitrogen) prepared in Tris-EDTA buffer as instructed by the manufacturer (5 μL SYBER gold in 50 mL Tris-EDTA), then incubated for 20 min at 80°C and cooled down to room temperature. Flow cytometric analysis was performed with excitation at 488- and 525-nm emission. For intracellular viral DNA quantification, 1 mL cells was collected by centrifugation (8000*g*, 3 min, 4°C) and washed twice in fresh media, and the DNA was released from cells using a REDExtract-N-Amp Plant PCR kit (Sigma-Aldrich) according to the manufacturer's instructions. The extract was diluted 100× in double distilled water, and 1 μL was used for quantitative PCR analysis with the major capsid protein (*mcp*) primers (Pagarete et al., 2009). All reactions were performed in biological triplicates and technical duplicates. For all reactions, Platinum SYBER Green qPCR SuperMix-UDG with ROX (Invitrogen) was used as described by the manufacturer. Reactions were performed on StepOnePlus real-time PCR systems (Applied Biosystems) as follows: 50°C for 2 min, 95°C for 2 min, 40 cycles of 95°C for 15 s, and 60°C for 30 s. Results were calibrated against serial dilutions of EhV201 DNA at known concentrations, enabling exact enumeration of viral abundance.

Cell Death Analysis

For cell death analysis, cells were stained with Sytox Green (Invitrogen) in DMSO at a final concentration of 1 μM. Samples were then incubated in

the dark for 1 h and analyzed by flow cytometry in the green channel (excitation 488 nm, emission 525 nm).

TEM

Culture (500 mL) was collected by centrifugation (8000*g*, 10 min, 20°C), resuspended in fixation media (2% glutaraldehyde, 4% paraformaldehyde, and 2% acrolein in artificial sea water [ASW]), and fixed for at least 24 h at 4°C. Cells were then washed in ASW and postfixed in 2% osmium tetroxide, 0.5% potassium dichromate, and 0.5% potassium hexacyanoferrate in ASW for 1 h at room temperature, washed again, and stained en block with 2% aqueous uranyl acetate for 1 h followed by ethanol dehydration. Samples were infiltrated with increasing concentrations of Epon EMBED 812 (EMS) and polymerized at 60°C. Thin sections (~70 nm) obtained with an Ultracut UCT microtome (Leica) were poststained with 2% uranyl acetate and Reynold's lead citrate and examined using FEI Tecnai T12 TEM operating at 120 kV. Images were recorded on an FEI Eagle 2Kx2K CCD camera.

RNA Isolation, Library Construction, and Sequencing

RNA was isolated from 500-mL cultures at time points as indicated with the RNeasy Plant Mini Kit (Qiagen) according to the manufacturer's instructions. The cDNA libraries were prepared following the manufacturer's instructions in the Illumina RNA sample preparation kit. Shortly, poly(T) oligo-attached magnetic beads were used to purify the poly(A)-containing mRNA molecules. The mRNA was fragmented into 200- to 500-bp pieces, and cleaved RNA fragments were converted into cDNA using SuperScript II reverse transcriptase (Life Technology) and random hexamer primers. Adaptors were ligated to the cDNA fragments, followed by purification, PCR, and an additional purification. The cDNA libraries were loaded onto a V2 flow cell, each sample on a single lane of the Illumina HiSequation 2000 sequencing platform, and 100-bp single-end reads were sequenced. The sequences were extracted using CASAVA v1.8.1 software (Illumina). Sequence reads were deposited in GenBank Short Read Archive with the study accession number SRP017794.

Transcriptome Assembly

Sequence reads were trimmed to a length of 90 bp, and adaptors were removed using the cutadapt program (Martin, 2011). The transcriptome assembly was performed by three combined approaches. The first one was de novo assembly performed with the CLC assembly cell (EMEA, Aarhus N) software, version 3.2.2. The second approach was genome and read based. Trimmed reads were mapped to an improved version of the available genome using TopHat software, version 1.3.0 (Trapnell et al., 2009), then Cufflinks (version 1.1.0) and Cuffcompare (Trapnell et al., 2010) were applied to define a list of transcripts that are comparable between all samples. Partial transcripts missed in this approach were extracted from TopHat alignments using Partek Genomics Suite software, version 6.5. The third approach used publicly available ESTs, downloaded from the National Center for Biotechnology Information (NCBI). The ESTs were clustered using TGICL version 2.1 (http://compbio.dfci.harvard.edu/tgi/software/). Additional clustering of potential transcripts was performed with TGICL, CD-HIT-EST (version 4.5.4) (Li and Godzik, 2006) or CAP3 (version date: 10/15/07) (Huang and Madan, 1999). Open reading frame extraction was performed using in-house Perl scripts.

Differential Expression and Clustering

Gene expression normalization was performed independently to the host and viral genomes. Transcript abundance estimation was performed using RSEM (Li and Dewey, 2011). Differentially expressed transcripts were identified by applying the algorithm suggested by Partek in http://www.partek.com/Tutorials/microarray/User_Guides/RNASEQ.pdf. The algorithm implementation was performed using an in-house R script. Differentially expressed genes (fold change >2 and false discovery rate <0.05 between any two conditions), that had four reads per million value >4 in at least one of the samples, were clustered into 13 clusters using the K-means algorithm. Examination of the possible difference between our transcript abundance estimation based on the log likelihood ratio and the DESeq program revealed strong correlation at the normalized read and fold change levels for differentially expressed genes between the two methods (Supplemental Table 10 and Supplemental Figure 9).

The distance matrix used for the clustering analysis was calculated using Pearson's dissimilarity. To measure the number of clusters that our transcriptomics data can well be classified into, the Davies-Bouldin index was used. The number of clusters was chosen based on the minimal index value to ensure a good separation between clusters and cluster homogeneity. This minimal value was manually inspected to ensure that the minimal index values reflect the biological variability in the data set.

Enrichment Analysis

GO annotations for the transcripts were obtained using Blast2GO (http://www.blast2go.com) (Conesa et al., 2005). GO enrichment analysis was performed using the Ontologizer 2.0 tool (http://compbio.charite.de/contao/index.php/ontologizer2.html) (Bauer et al., 2008). KEGG and KOG annotations were obtained by submitting the longest open reading frame protein sequence for each transcript to the WebMGA server (http://weizhonglab.ucsd.edu/metagenomic-analysis/) (Wu et al., 2011). KEGG and KOG gene counts per term and/or cluster were performed using in-house Perl scripts. Enrichment P values were calculated by applying the hypergeometric test in R.

Annotation and Expression Level of Genes Encoding Enzymes Involved in Sphingolipid Metabolism

The target protein sequence from human, yeast, and *Arabidopsis thaliana* was compared with the *E. huxleyi* genome with TBlastN at the Joint Genome Initiative (http://genome.jgi-psf.org/pages/blast.jsf?db=Emihu1) with the following parameters: target database: Emiliania huxleyi v1 scaffolds (unmasked), "filter low complexity regions" off, and "perform gapped alignment" on. Hits from the various input species were compared, and the best genomic locus was chosen. If ESTs were available, they were used to construct the transcript. If there was incomplete or no coverage with ESTs, gene prediction was performed manually on the basis of the BLAST results. If no genomic locus was found, or if the genome was incomplete in the locus, BLAST searches were performed at NCBI against the *E. huxleyi* EST collection directly. When the reads were sequenced, they were also used as a basis for gene definition and for refinement of existing gene definitions. After the best locus was defined, the process was repeated on the rest of the loci to determine all family members, and then multiple alignments and phylogenetic analyses were performed to ensure that the correct homolog was chosen. If there were no hits with any of the three input species, the target sequence from other species was used. The Blat tool (Kent, 2002) was used to match manually defined genes and automatically defined transcripts. In cases where several transcripts matched one gene due to different isoforms or transcripts that partially covered the entire gene, the normalized reads of all the transcripts matching the gene were summed.

RT-PCR Analysis

Equal amounts of RNA were used for cDNA synthesis with the ThermoScript RT-PCR system (Invitrogen). For transcript abundance analysis, Platinum SYBER Green qPCR SuperMix-UDG with ROX (Invitrogen) was used as described by the manufacturer. Reactions were performed on StepOnePlus real-time PCR systems (Applied Biosystems) as follows: 50°C for 2 min, 95°C for 2 min, 40 cycles of 95°C for 15 s, and 60°C for 30 s. Transcript abundance was calculated using the comparative δ-δ-Ct method. Primers for viral *SPT*

and *DCD* were used as by Pagarete et al. (2009). A list of primers for detecting transcripts of viral *SPT*, *DCD*, and *CerS* and host *GBA*, *SPHK*, *UGCG*, and *tubulin* are listed in Supplemental Table 11. The *tubulin* gene was used as a reference for equalizing the levels of RNA.

Solvents

Solvents used for metabolite extraction and sample preparation were methanol, pyridine, water (all Chromasolv Plus; Sigma-Aldrich), ethanol, and chloroform (both HPLC grade; JT Baker).

Intracellular Metabolite Extraction

Intracellular metabolite samples (culture or medium) were taken and treated identically. Briefly, 2× 100 mL (two analytical replicates) per sample were quickly concentrated on 47-mm GF/C filters (Whatman) while applying a vacuum (~500 mbar). The extraction procedure, work-up, and measurement were based on a protocol by Vidoudez and Pohnert (2012) with the following adaptations: samples of each time point (4, 24, 32, and 48 hpi) were derivatized in one batch, extracts corresponding to an equivalent of $\sim 50 \cdot 10^6$ cells were transferred to an Eppendorf centrifuge tube and filled with extraction mix (methanol:ethanol:chloroform, 1:3:1, v:v at −20°C) to a total volume of 1 mL. If insufficient cells were available, the whole sample was used and adjusted to 1 mL. In the first derivatization step, we added only 25 μL methoxyamine solution (10 mg methoxyamine hydrochloride in 0.5 mL pyridine; Sigma-Aldrich) and increased the incubation at room temperature to 10 h. After the second derivatization step, samples were transferred to 200-μL glass inserts and centrifuged for 5 min at 8000*g*. The supernatant was then transferred to new glass inserts and measured within 24 h by GC-MS. The applied extraction protocol successfully covers several metabolic classes, including fatty acids and sterols, which possess a recovery rate of >80% (Vidoudez and Pohnert, 2012).

GC-MS Analysis

Batches (20 samples) were measured in random order on an Agilent 6890N gas chromatograph equipped with a 30-m DB-5ms column (0.25-mm internal diameter, 0.25-μm film thickness, with 8-m Duraguard precolumn; Agilent) and He 5.0 as carrier gas at a constant flow rate of 1 mL min^{-1}. After each batch, the liner (deactivated glass liner 4 × 6.3 × 78.5 mm; Agilent) was exchanged. For detection, a GCT premier (Waters) orthogonal reflectron time-of-flight mass spectrometer was used. One microliter per sample was injected at 300°C in split mode 1. GC-MS parameters were: initial temperature of 60°C for 1 min followed by an increase of 15°C min^{-1} to a final temperature of 310°C (held for 10 min). The mass spectrometry scan rate was set to 2 scans s^{-1} in dynamic range extension mode and the electron impact source at 70 eV. The resolution of the tune was ≥5800 at *m/z* 501.97. A quality control standard (test standard, DB-5ms [Capillary/Megabore]; Agilent) was measured before and after each batch.

Metabolome Data Processing

For data processing, each sampling point (4, 24, 32, and 48 hpi) was treated separately. We used the Component Detection Algorithm in MassLynx (version 4.1; Waters) for background noise correction with mass chromatographic quality set at 0.65 and a smoothing window of three scans. Chromatograms were converted to netCDF files by a MassLynx DataBridge and each sampling point processed separately in AMDIS (version 2.71, NIST, http://chemdata.nist.gov/, 2012) followed by peak integration in MET-IDEA (version 2.08, http://bioinfo.noble.org/download/, 2012) (Lei et al., 2012) as described by Vidoudez and Pohnert (2012). We modified the component width to 20 in AMDIS and accepted a mass limit of 50 in MET-IDEA in a few cases where no suitable ion was found. Peak integration was inspected and manually corrected. The resulting data matrix was copied into Excel 2010 (Microsoft). We excluded signals of the retention time index, ribitol, with a retention time <5 min, and a few signals regarded as noise or contamination after manual inspection. The mean of peak areas from the same biological replicate was used. If a signal was detected in the medium, it was subtracted 3× from the corresponding signal in all samples and excluded, if afterwards all peak areas of a signal were below zero. Data were normalized by peak sums to avoid the effects of differing signal intensities due to variations in the extracted cells. The final data matrix was exported as a text file for statistical analysis.

Statistical Analysis of Metabolome Data

Differences between control and cells infected by either virus were evaluated by CAP, which is based on a discriminant analysis after an initial principal coordinate analysis, using CAP12 software (Anderson and Willis, 2003) with parameters as defined by Vidoudez and Pohnert (2012). Pairs of the retention time and mass to charge ratio (*m/z*) as found during data analysis constituted the explanatory variable (X) and the peak area of each metabolite the responsive variable (Y). These variables were not interchangeable. This analysis was chosen because it was previously successfully applied in microalgae metabolomics, it has the advantage of being not very sensitive to hidden correlations, as should be expected with metabolic samples that contain amine derivatives, and the software is generally available in contrast to other approaches (Baran et al., 2006). Sample coordinates of the CAP output file were visualized graphically in SigmaPlot (version 11.0; Systat Software).

Metabolite Identification

Mass spectra of each compound were manually examined using MS search software (version 2.0 d; NIST) with the following implemented libraries: NIST library version 2005, T_MSRI_ID 2004-03-01, GMD_20111121_VAR5_ALK_MSP (http://csbdb.mpimp-golm.mpg.de/csbdb/gmd/msri/gmd_msri.html and http://gmd.mpimp-golm.mpg.de/, both Golm Metabolome Database) (Wagner et al., 2003; Hummel et al., 2010), and an in-house library. A few peaks of interest were searched against MassFinder 4.0 (http://massfinder.com/wiki/Terpenoids_Library_List). A structure was accepted if several criteria were met: reverse match factor >800, retention index of the suggested structure similar to retention time of the compound, and, if a standard was available, compound and standard identical in spectrum and retention time.

Peaks of metabolites of specific interest not picked up by AMDIS were manually integrated using a selected trace ion and the QuanLynx tool incorporated in MassLynx (version 4.1; Waters). After processing as described above, peak areas were added to the constrained analysis.

Analysis of Free Metabolites in Viral Capsids

Viral lysate (3 l) of *E. huxleyi* were concentrated on a 50-kD tangential flow filtration system (Millipore). Viruses were separated by an OptiPrep gradient (25 to 40%; according to Lawrence and Steward, 2010) and washed three times on a 50-kD Amicon filter (Millipore). Concentrated viruses were suspended in 200 μL PBS and kept at 4°C until further analysis. Therefore, viruses were retained on 25-mm Anodisc 25 filters (0.02 μm pore size; Whatman) and extracted together with a sample of k/2 medium as described above with slight modifications: 500 μL extraction mix was used, the whole sample was derivatized, 50 μL methoxyamine solution (20 mg methoxyamine hydrochloride in 1 mL pyridine; Sigma-Aldrich) was added for the first derivatization step, and a glass wool containing liner was used for GC-MS measurement. Resulting chromatograms of viral metabolites were screened and spectra were compared with library entries using the MS search as described above.

Sphingolipid Analysis

Lipids were extracted from *E. huxleyi* cells infected with either EhV201 (lytic) or EhV163 (nonlytic) and from noninfected cells harvested at 1, 4, 24,

32, and 48 hpi in three biological replicates of 50 mL. Lipid analysis was performed as previously described (Hummel et al., 2011) with some modifications: GF/F filters containing algae were placed in 15-mL glass tubes and extracted with 3 mL of precooled (−20°C) homogenous methanol:methyl-tert-butyl-ether (1:3, v/v) mixture containing 0.1 μg/mL of Lactosyl Ceramide (d18:1/12:0) (Avanti), which was used as internal standard. The tubes were shaken for 20 min at 4°C and then sonicated for 30 min. Ultraperformance liquid chromatography (UPLC)–grade water:methanol (3:1, v/v) solution (1.5 mL) was added to the tubes followed by centrifugation. The upper organic phase (1.2 mL) was transferred into 2-mL Eppendorf tubes. The polar phase was reextracted with 0.5 mL of TMBE for better lipid recovery efficiency. Organic phases were combined and dried under a nitrogen stream and then stored at −80°C until analysis.

UPLC–Mass Spectrometry Analysis

Lipids were separated and analyzed using an UPLC Aquity instrument combined with a q-TOF Synapt G2S mass analyzer (Waters). Chromatographic conditions were as described by Hummel et al. (2011). The electrospray probe was operated at 2 kV and the cone was set to 40 V. The source and desolvation temperatures were 120 and 550°C, respectively. Samples were injected in the MSe mode, using a collision energy ramp of 15 to 35 eV. Mass spectra were collected in the positive ion mode. MassLynx (version 4.1; Waters) was used to control the instrument and calculate accurate masses.

Data Analysis

The metabolites were integrated using the QuanLynx tool incorporated in MassLynx. Areas of metabolites were normalized to the area of the IS and to the amount of algae used for analysis. Detection of vGSL, hGSL, and sGSL was made according to Vardi et al. (2009), Vardi et al. (2012), and Fulton et al. (2014).

Correlation Metabolome-Transcriptome

For correlating transcript levels with specific metabolite levels, we used the free statistical computing environment R (www.r-project.org), with the weighted correlation network analysis package as described by Langfelder and Horvath (2008). In order to assess the range of correlation values that have biological meaning, we estimated both the lowest correlation values that need to be considered. Both the transcript and metabolite data sets were randomized and analyzed for correlation a hundred times. The permutation test's average correlation score was near zero (average = 0.17, σ = 0.02). Thus, if correlation values are distributed normally, values beyond 3.2906σ have only a 0.1% chance of being random. Hence, only values below −0.3 or above 0.3 should be considered as significant. Network visualization that holds only highly significant correlation values (absolute r-value > 0.7) is presented as Supplemental Figure 4.

Accession Numbers

Sequence reads were deposited to NCBI's Short Read Archive under accession number SRP017794. Manually curated genes that belong to the sphingolipid biosynthetic pathway can be found in the GenBank database under the following accession numbers: *SPT*, KJ868221; *CerS*, KJ868222; *DCD*, KJ868223; *SPHK*, KJ868224; *S1PP*, KJ868225; *UGCG1*, KJ868227; *UGCG2*, KJ868228; *GBA*, KJ868229; *Ceramidase1*, KJ868230; *Ceramidase2*, KJ868231; *Ceramidase3*, KJ868232; *Ceramidase4*, KJ868233; and *Ceramidase5*, KJ868234.

Supplemental Data

The following materials are available in the online version of this article.

Supplemental Figure 1. Scheme of Experimental Design and Workflow.

Supplemental Figure 2. Induction of Pentose Phosphate Pathway and Nucleotide Biosynthesis during Viral Infection.

Supplemental Figure 3. Visualization of RNA-seq Reads Mapped to the Whole EhV Genome at 1 hpi.

Supplemental Figure 4. Network Visualization of Correlation Coefficient Values between Gene Cluster Profiles and Metabolite Abundance.

Supplemental Figure 5. Effect of Fatty Acid Biosynthesis Inhibition by C75 on Host Abundance and Viral DNA Production.

Supplemental Figure 6. Expression Patterns of Specific Sphingolipid Metabolism Genes Analyzed by RT-PCR.

Supplemental Figure 7. Viral Production Is Not Affected by Inhibition of the Methylerythritol Phosphate Pathway.

Supplemental Figure 8. Effect of Mevalonate Pathway Inhibition by Cerivastatin on Host Abundance and Viral DNA Production.

Supplemental Figure 9. Correlation Coefficient Values between Fold-Change Values Calculated Using the DESeq Program and the Log Likelihood Ratio (LLR) Suggested by Partek.

Supplemental Data Set 1. Summary of Illumina RNA-seq Reads Obtained and Their Mapping to *E. huxleyi* and EhV Genomes.

Supplemental Data Set 2. Functional Analysis of Enriched KEGG Pathways and KOG Categories.

Supplemental Data Set 3. Average Number of Detected Metabolites.

Supplemental Data Set 4. Fold Change of Metabolites Detected during Viral Infection.

Supplemental Data Set 5. Statistical Support Values of CAP.

Supplemental Data Set 6. Metabolites Discriminating between Lytic and Nonlytic Infected Cells from Control Cells at Each Time Point.

Supplemental Data Set 7. Correlation Coefficient Values between Gene Cluster Profiles and Metabolite Abundance.

Supplemental Data Set 8. Expression Level of Host and Viral Genes Encoding Enzymes Involved in Sphingolipid Metabolism.

Supplemental Data Set 9. Metabolites Identified in Concentrated, Purified EhV201 Virions.

Supplemental Data Set 10. Correlation Coefficient Values between Fold-Change and RPM Values Calculated Using the DESeq Program and the Log Likelihood Ratio (LLR) Approach.

Supplemental Data Set 11. Sequences of Primers Used for qPCR Analysis.

Supplemental Data Set 12. Abbreviations of Enzyme Names.

ACKNOWLEDGMENTS

This research was supported by the European Research Council StG (INFOTROPHIC Grant 280991), the Israeli Science Foundation Legacy Heritage fund (Grant 1716/09), International Reintegration Grant–Marie Curie grant, and the generous support of Edith and Nathan Goldenberg Career Development Chair awarded to A.V. M.A.M. thanks the International Leibniz Research School for Microbial and Bimolecular Interactions and the Minerva Stiftung of the Max-Plank-Gesellschaft. G.P. and M.A.M. acknowledge funding by the Volkswagen Foundation.

AUTHOR CONTRIBUTIONS

S.R., M.A.M., G.P., and A.V. designed and performed research, analyzed data, contributed analytical tools, and wrote the article. D.S. designed

and performed research. U.S., E.W., and S.M. performed research. S.M. and A.A. contributed analytical tools, and O.T. contributed new computational tools. S.B.-D. and E.F. contributed new computational tools and analyzed data.

Received March 25, 2014; revised May 7, 2014; accepted May 26, 2014; published June 10, 2014.

REFERENCES

Allen, M.J., Martinez-Martinez, J., Schroeder, D.C., Somerfield, P.J., and Wilson, W.H. (2007). Use of microarrays to assess viral diversity: from genotype to phenotype. Environ. Microbiol. **9:** 971–982.

Allen, M.J., Forster, T., Schroeder, D.C., Hall, M., Roy, D., Ghazal, P., and Wilson, W.H. (2006b). Locus-specific gene expression pattern suggests a unique propagation strategy for a giant algal virus. J. Virol. **80:** 7699–7705.

Allen, M.J., Schroeder, D.C., Donkin, A., Crawfurd, K.J., and Wilson, W.H. (2006a). Genome comparison of two Coccolithoviruses. Virol. J. **3:** 15.

Anderson, M.J., and Willis, T.J. (2003). Canonical analysis of principal coordinates: a useful method of constrained ordination for ecology. Ecology **84:** 511–525.

Arslan, D., Legendre, M., Seltzer, V., Abergel, C., and Claverie, J.-M. (2011). Distant Mimivirus relative with a larger genome highlights the fundamental features of Megaviridae. Proc. Natl. Acad. Sci. USA **108:** 17486–17491.

Baran, R., Kochi, H., Saito, N., Suematsu, M., Soga, T., Nishioka, T., Robert, M., and Tomita, M. (2006). MathDAMP: a package for differential analysis of metabolite profiles. BMC Bioinformatics **7:** 530.

Bauer, S., Grossmann, S., Vingron, M., and Robinson, P.N. (2008). Ontologizer 2.0—a multifunctional tool for GO term enrichment analysis and data exploration. Bioinformatics **24:** 1650–1651.

Berkey, R., Bendigeri, D., and Xiao, S. (2012). Sphingolipids and plant defense/disease: the "death" connection and beyond. Front. Plant Sci. **3:** 68.

Bidle, K.D., Haramaty, L., Barcelos E Ramos, J., and Falkowski, P. (2007). Viral activation and recruitment of metacaspases in the unicellular coccolithophore, *Emiliania huxleyi.* Proc. Natl. Acad. Sci. USA **104:** 6049–6054.

Blanc, M., et al. (2011). Host defense against viral infection involves interferon mediated down-regulation of sterol biosynthesis. PLoS Biol. **9:** e1000598.

Bratbak, G., Egge, J.K., and Heldal, M. (1993). Viral mortality of the marine alga *Emiliania huxleyi* (Haptophyceae) and termination of algal blooms. Mar. Ecol. Prog. Ser. **93:** 39–48.

Chipuk, J.E., McStay, G.P., Bharti, A., Kuwana, T., Clarke, C.J., Siskind, L.J., Obeid, L.M., and Green, D.R. (2012). Sphingolipid metabolism cooperates with BAK and BAX to promote the mitochondrial pathway of apoptosis. Cell **148:** 988–1000.

Conesa, A., Götz, S., García-Gómez, J.M., Terol, J., Talón, M., and Robles, M. (2005). Blast2GO: a universal tool for annotation, visualization and analysis in functional genomics research. Bioinformatics **21:** 3674–3676.

DeAngelis, P.L., Jing, W., Graves, M.V., Burbank, D.E., and Van Etten, J.L. (1997). Hyaluronan synthase of chlorella virus PBCV-1. Science **278:** 1800–1803.

Delgado, T., Sanchez, E.L., Camarda, R., and Lagunoff, M. (2012). Global metabolic profiling of infection by an oncogenic virus: KSHV induces and requires lipogenesis for survival of latent infection. PLoS Pathog. **8:** e1002866.

Disch, A., Schwender, J., Müller, C., Lichtenthaler, H.K., and Rohmer, M. (1998). Distribution of the mevalonate and glyceraldehyde phosphate/pyruvate pathways for isoprenoid biosynthesis in unicellular algae and the cyanobacterium *Synechocystis* PCC 6714. Biochem. J. **333:** 381–388.

Enav, H., Mandel-Gutfreund, Y., and Béjà, O. (2014). Comparative metagenomic analyses reveal viral-induced shifts of host metabolism towards nucleotide biosynthesis. Microbiome **2:** 9.

Evans, C., Malin, G., Mills, G.P., and Wilson, W.H. (2006). Viral infection of *Emiliania huxleyi* (Prymnesiophyceae) leads to elevated production of reactive oxygen species. J. Phycol. **42:** 1040–1047.

Evans, C., Pond, D.W., and Wilson, W.H. (2009). Changes in *Emiliania huxleyi* fatty acid profiles during infection with *E. huxleyi* virus 86: physiological and ecological implications. Aquat. Microb. Ecol. **55:** 219–228.

Feldmesser, E., Rosenwasser, S., Vardi, A., and Ben-Dor, S. (2014). Improving transcriptome construction in non-model organisms: integrating manual and automated gene definition in *Emiliania huxleyi.* BMC Genomics **15:** 148.

Field, C.B., Behrenfeld, M.J., Randerson, J.T., and Falkowski, P. (1998). Primary production of the biosphere: integrating terrestrial and oceanic components. Science **281:** 237–240.

Frada, M., Probert, I., Allen, M.J., Wilson, W.H., and de Vargas, C. (2008). The "Cheshire Cat" escape strategy of the coccolithophore *Emiliania huxleyi* in response to viral infection. Proc. Natl. Acad. Sci. USA **105:** 15944–15949.

Fuhrman, J.A. (1999). Marine viruses and their biogeochemical and ecological effects. Nature **399:** 541–548.

Fulton, J.M., Fredricks, H.F., Bidle, K.D., Vardi, A., Kendrick, B.J., DiTullio, G.R., and Van Mooy, B.A.S. (2014). Novel molecular determinants of viral susceptibility and resistance in the lipidome of *Emiliania huxleyi.* Environ. Microbiol. **16:** 1137–1149.

Han, G., Gable, K., Yan, L., Allen, M.J., Wilson, W.H., Moitra, P., Harmon, J.M., and Dunn, T.M. (2006). Expression of a novel marine viral single-chain serine palmitoyltransferase and construction of yeast and mammalian single-chain chimera. J. Biol. Chem. **281:** 39935–39942.

Hartmann, M.-A. (1998). Plant sterols and the membrane environment. Trends Plant Sci. **3:** 170–175.

Holligan, P., et al. (1993). A biogeochemical study of the coccolithophore, *Emiliania huxleyi,* in the North Atlantic. Global Biogeochem. Cycles **7:** 879–900.

Huang, X., and Madan, A. (1999). CAP3: A DNA sequence assembly program. Genome Res. **9:** 868–877.

Hummel, J., Segu, S., Li, Y., Irgang, S., Jueppner, J., and Giavalisco, P. (2011). Ultra performance liquid chromatography and high resolution mass spectrometry for the analysis of plant lipids. Front. Plant Sci. **2:** 54.

Hummel, J., Strehmel, N., Selbig, J., Walther, D., and Kopka, J. (2010). Decision tree supported substructure prediction of metabolites from GC-MS profiles. Metabolomics **6:** 322–333.

Hurst, C.J. (2011). An introduction to viral taxonomy with emphasis on microbial and botanical hosts and the proposal of Akamara, a potential domain for the genomic acellular agents. In Studies in Viral Ecology: Microbial and Botanical Host Systems, J.C. Hurst, ed (Hoboken, New Jersey: John Wiley a Sons), pp. 41–65.

Hurwitz, B.L., Hallam, S.J., and Sullivan, M.B. (2013). Metabolic reprogramming by viruses in the sunlit and dark ocean. Genome Biol. **14:** R123.

Iglesias-Rodriguez, M.D., et al. (2008). Phytoplankton calcification in a high-CO_2 world. Science **320:** 336–340.

Kapadia, S.B., and Chisari, F.V. (2005). Hepatitis C virus RNA replication is regulated by host geranylgeranylation and fatty acids. Proc. Natl. Acad. Sci. USA **102:** 2561–2566.

Kegel, J.U., Blaxter, M., Allen, M.J., Metfies, K., Wilson, W.H., and Valentin, K. (2010). Transcriptional host-virus interaction of *Emiliania*

huxleyi (Haptophyceae) and EhV-86 deduced from combined analysis of expressed sequence tags and microarrays. Eur. J. Phycol. **48:** 1–12.

Keller, M.D., Selvin, R.C., Claus, W., and Guillard, R.R.L. (1987). Media for the culture of oceanic ultraphytoplankton. J. Phycol. **23:** 633–638.

Kent, W.J. (2002). BLAT—the BLAST-like alignment tool. Genome Res. **12:** 656–664.

Langfelder, P., and Horvath, S. (2008). WGCNA: an R package for weighted correlation network analysis. BMC Bioinformatics **9:** 559.

Lawrence, J.E., and Steward, G.F. (2010). Purification of viruses by centrifugation. In Manual of Aquatic Viral Ecology, S.W. Wilhelm, M.G. Weinbauer, and C.A. Suttle, eds (Waco, TX: ASLO), pp. 166–181.

Lei, Z., Li, H., Chang, J., Zhao, P.X., and Sumner, L.W. (2012). MET-IDEA version 2.06; improved efficiency and additional functions for mass spectrometry-based metabolomics data processing. Metabolomics **8:** 105–110.

Li, B., and Dewey, C.N. (2011). RSEM: accurate transcript quantification from RNA-Seq data with or without a reference genome. BMC Bioinformatics **12:** 323.

Li, W., and Godzik, A. (2006). Cd-hit: a fast program for clustering and comparing large sets of protein or nucleotide sequences. Bioinformatics **22:** 1658–1659.

Liang, H., Yao, N., Song, J.T., Luo, S., Lu, H., and Greenberg, J.T. (2003). Ceramides modulate programmed cell death in plants. Genes Dev. **17:** 2636–2641.

Lindell, D., Jaffe, J.D., Johnson, Z.I., Church, G.M., and Chisholm, S.W. (2005). Photosynthesis genes in marine viruses yield proteins during host infection. Nature **438:** 86–89.

Mackenzie, J.M., Khromykh, A.A., and Parton, R.G. (2007). Cholesterol manipulation by West Nile virus perturbs the cellular immune response. Cell Host Microbe **2:** 229–239.

Mackinder, L.C.M., Worthy, C.A., Biggi, G., Hall, M., Ryan, K.P., Varsani, A., Harper, G.M., Wilson, W.H., Brownlee, C., and Schroeder, D.C. (2009). A unicellular algal virus, *Emiliania huxleyi* virus 86, exploits an animal-like infection strategy. J. Gen. Virol. **90:** 2306–2316.

Martin, M. (2011). Cutadapt removes adapter sequences from high-throughput sequencing reads. EMBnet J. **17:** 10–12.

Mason, R.P. (2006). Molecular basis of differences among statins and a comparison with antioxidant vitamins. Am. J. Cardiol. **98** (11A)**:** 34P–41P.

Maxwell, J.R., Mackenzie, A.S., and Volkman, J.K. (1980). Configuration at C-24 in steranes and sterols. Nature **286:** 694–697.

Monier, A., Pagarete, A., de Vargas, C., Allen, M.J., Read, B., Claverie, J.-M., and Ogata, H. (2009). Horizontal gene transfer of an entire metabolic pathway between a eukaryotic alga and its DNA virus. Genome Res. **19:** 1441–1449.

Mullen, T.D., and Obeid, L.M. (2012). Ceramide and apoptosis: explorinig the enigmatic connections between spingolipid metabolism and programmed cell death. Anticancer Agents Med. Chem. **12:** 340–363.

Müller, D.G., Kapp, M., and Knippers, R. (1998). Viruses in marine brown algae. In Advances in Virus Research, K. Maramorosch, F.A. Murphy, and A.J. Shatkin, eds (New York: Academic Press), pp. 49–67.

Munger, J., Bennett, B.D., Parikh, A., Feng, X.-J., McArdle, J., Rabitz, H.A., Shenk, T., and Rabinowitz, J.D. (2008). Systems-level metabolic flux profiling identifies fatty acid synthesis as a target for antiviral therapy. Nat. Biotechnol. **26:** 1179–1186.

Nissimov, J.I., Worthy, C.A., Rooks, P., Napier, J.A., Kimmance, S.A., Henn, M.R., Ogata, H., and Allen, M.J. (2012). Draft genome sequence of four coccolithoviruses: *Emiliania huxleyi* virus EhV-88, EhV-201, EhV-207, and EhV-208. J. Virol. **86:** 2896–2897.

Overmeyer, J.H., and Maltese, W.A. (1992). Isoprenoid requirement for intracellular transport and processing of murine leukemia virus envelope protein. J. Biol. Chem. **267:** 22686–22692.

Pagarete, A., Allen, M.J., Wilson, W.H., Kimmance, S.A., and de Vargas, C. (2009). Host-virus shift of the sphingolipid pathway along an *Emiliania huxleyi* bloom: survival of the fattest. Environ. Microbiol. **11:** 2840–2848.

Pagarete, A., Le Corguillé, G., Tiwari, B., Ogata, H., de Vargas, C., Wilson, W.H., and Allen, M.J. (2011). Unveiling the transcriptional features associated with coccolithovirus infection of natural *Emiliania huxleyi* blooms. FEMS Microbiol. Ecol. **78:** 555–564.

Read, B.A., et al; Emiliania huxleyi Annotation Consortium (2013). Pan genome of the phytoplankton *Emiliania* underpins its global distribution. Nature **499:** 209–213.

Roossinck, M.J. (1997). Mechanisms of plant virus evolution. Annu. Rev. Phytopathol. **35:** 191–209.

Schauer, N., and Fernie, A.R. (2006). Plant metabolomics: towards biological function and mechanism. Trends Plant Sci. **11:** 508–516.

Schroeder, D.C., Oke, J., Malin, G., and Wilson, W.H. (2002). Coccolithovirus (Phycodnaviridae): characterisation of a new large dsDNA algal virus that infects *Emiliana huxleyi*. Arch. Virol. **147:** 1685–1698.

Selstam, E., and Jackson, A.O. (1983). Lipid composition of sonchus yellow net virus. J. Gen. Virol. **64:** 1607–1613.

Sharon, I., Alperovitch, A., Rohwer, F., Haynes, M., Glaser, F., Atamna-Ismaeel, N., Pinter, R.Y., Partensky, F., Koonin, E.V., Wolf, Y.I., Nelson, N., and Béjà, O. (2009). Photosystem I gene cassettes are present in marine virus genomes. Nature **461:** 258–262.

Simó, R. (2001). Production of atmospheric sulfur by oceanic plankton: biogeochemical, ecological and evolutionary links. Trends Ecol. Evol. (Amst.) **16:** 287–294.

Spiegel, S., and Milstien, S. (2003). Sphingosine-1-phosphate: an enigmatic signalling lipid. Nat. Rev. Mol. Cell Biol. **4:** 397–407.

Suttle, C.A. (2007). Marine viruses—major players in the global ecosystem. Nat. Rev. Microbiol. **5:** 801–812.

Thompson, L.R., Zeng, Q., Kelly, L., Huang, K.H., Singer, A.U., Stubbe, J., and Chisholm, S.W. (2011). Phage auxiliary metabolic genes and the redirection of cyanobacterial host carbon metabolism. Proc. Natl. Acad. Sci. USA **108:** E757–E764.

Trapnell, C., Pachter, L., and Salzberg, S.L. (2009). TopHat: discovering splice junctions with RNA-Seq. Bioinformatics **25:** 1105–1111.

Trapnell, C., Williams, B.A., Pertea, G., Mortazavi, A., Kwan, G., van Baren, M.J., Salzberg, S.L., Wold, B.J., and Pachter, L. (2010). Transcript assembly and quantification by RNA-Seq reveals unannotated transcripts and isoform switching during cell differentiation. Nat. Biotechnol. **28:** 511–515.

Van Etten, J.L., Graves, M.V., Müller, D.G., Boland, W., and Delaroque, N. (2002). *Phycodnaviridae*—large DNA algal viruses. Arch. Virol. **147:** 1479–1516.

Vardi, A., Haramaty, L., Van Mooy, B.A.S., Fredricks, H.F., Kimmance, S.A., Larsen, A., and Bidle, K.D. (2012). Host-virus dynamics and subcellular controls of cell fate in a natural coccolithophore population. Proc. Natl. Acad. Sci. USA **109:** 19327–19332.

Vardi, A., Van Mooy, B.A., Fredricks, H.F., Popendorf, K.J., Ossolinski, J.E., Haramaty, L., and Bidle, K.D. (2009). Viral glycosphingolipids induce lytic infection and cell death in marine phytoplankton. Science **326:** 861–865.

Vastag, L., Koyuncu, E., Grady, S.L., Shenk, T.E., and Rabinowitz, J.D. (2011). Divergent effects of human cytomegalovirus and herpes simplex virus-1 on cellular metabolism. PLoS Pathog. **7:** e1002124.

Vidoudez, C., and Pohnert, G. (2012). Comparative metabolomics of the diatom *Skeletonema marinoi* in different growth phases. Metabolomics **8:** 654–669.

Wagner, C., Sefkow, M., and Kopka, J. (2003). Construction and application of a mass spectral and retention time index database generated from plant GC/EI-TOF-MS metabolite profiles. Phytochemistry **62:** 887–900.

Westermann, A.J., Gorski, S.A., and Vogel, J. (2012). Dual RNA-seq of pathogen and host. Nat. Rev. Microbiol. **10:** 618–630.

Wilson, W.H., Tarran, G.A., Schroeder, D.C., Cox, M., Oke, J., and Malin, G. (2002). Isolation of viruses responsible for the demise of an *Emiliania huxleyi* bloom in the English Channel. J. Mar. Biol. Assoc. U. K. **82:** 369–377.

Wilson, W.H., et al. (2005). Complete genome sequence and lytic phase transcription profile of a *Coccolithovirus.* Science **309:** 1090–1092.

Wu, S., Zhu, Z., Fu, L., Niu, B., and Li, W. (2011). WebMGA: a customizable web server for fast metagenomic sequence analysis. BMC Genomics **12:** 444.

Ye, J., Wang, C., Sumpter, R., Jr., Brown, M.S., Goldstein, J.L., and Gale, M., Jr.,. (2003). Disruption of hepatitis C virus RNA replication through inhibition of host protein geranylgeranylation. Proc. Natl. Acad. Sci. USA **100:** 15865–15870.

Yeh, E., and DeRisi, J.L. (2011). Chemical rescue of malaria parasites lacking an apicoplast defines organelle function in blood-stage *Plasmodium falciparum.* PLoS Biol. **9:** e1001138.

Yutin, N., and Koonin, E.V. (2009). Evolution of DNA ligases of nucleo-cytoplasmic large DNA viruses of eukaryotes: a case of hidden complexity. Biol. Direct **4:** 51.

Zeng, Q., and Chisholm, S.W. (2012). Marine viruses exploit their host's two-component regulatory system in response to resource limitation. Curr. Biol. **22:** 124–128.

Zhao, N., Wang, G., Norris, A., Chen, X., and Chen, F. (2013). Studying plant secondary metabolism in the age of genomics. Crit. Rev. Plant Sci. **32:** 369–382.

Rewiring Host Lipid Metabolism by Large Viruses Determines the Fate of *Emiliania huxleyi*, a Bloom-Forming Alga in the Ocean

Shilo Rosenwasser, Michaela A. Mausz, Daniella Schatz, Uri Sheyn, Sergey Malitsky, Asaph Aharoni, Eyal Weinstock, Oren Tzfadia, Shifra Ben-Dor, Ester Feldmesser, Georg Pohnert and Assaf Vardi

Plant Cell 2014;26;2689-2707; originally published online June 10, 2014;
DOI 10.1105/tpc.114.125641